CEAS Space Journal
https://doi.org/10.1007/s12567-026-00699-y

ORIGINAL PAPER

Characterizing clock-induced errors in laser-communication-based inter-satellite ranging

Rashika Jain[1] · Dominic Dirkx[1] · Stefano Speretta[1]

Received: 19 September 2025 / Revised: 18 November 2025 / Accepted: 8 January 2026

Abstract
High-precision inter-satellite ranging is critical for formation flying, autonomous navigation, and scientific measurements in small-satellite missions. Laser communication terminals (LCTs) offer an opportunity to perform both data transfer and ranging, but their dual-use imposes stringent requirements on onboard clocks and timing electronics. This paper investigates the impact of clock-induced timing errors on two-way LCT-based ranging between CubeSats operating around the near-Earth asteroid 99942 Apophis. A methodology is developed to unify clock noise specifications provided in datasheets, generating realistic timing errors across microsecond-to-hour integration periods. Using high-fidelity orbital simulations, two orbital configurations—coplanar and non-coplanar—are analyzed to evaluate how relative satellite geometry influences the propagation of clock errors into range measurements, orbit determination, and the estimation of Apophis' gravitational parameter. Results demonstrate that inter-satellite links (ISLs) can reduce orbit determination errors along directions weakly constrained by Earth-based Doppler—from 1–3 m to 0.1–0.3 m in coplanar formations, and even further in non-coplanar formations—corresponding to improvements of one to two orders of magnitude. Subsystem-level noise, such as detector jitter and time tagging, can still limit achievable precision, even with high-performance clocks. The methodology provides a framework applicable to a broad range of small-satellite missions, guiding the selection of clocks, formation geometry, and system design to optimize both navigation performance and science return.

Keywords Laser communication terminal · Data-aided ranging · Two-way ranging · Clock noise modeling · Inter-satellite links · Small-body missions

1 Introduction

Accurate relative distance measurements are fundamental to satellite formation flying, enabling precise coordinated maneuvers, Earth observation, scientific interferometry, and deep-space exploration [1]. These measurements rely on ranging techniques, which determine distance by measuring the change in phase, frequency, or time of the signals exchanged between satellites [2]. Achieving high-precision ranging requires highly accurate timing systems, typically sub-ns-level accuracy for resolving sub-meter or even centimeter-scale changes in inter-satellite separation.

For small satellites, integrating dedicated ranging subsystems is challenging due to strict constraints on size, mass and power (SMaP). Consequently, there is growing interest in leveraging existing communication terminals not only for data transfer, but also for ranging functionalities. A similar trend has already taken place in radio-frequency (RF) systems, where the communication link served as the only available means to reach the satellite and was therefore adapted to support both telemetry and tracking [3–8]. This dual-use approach can reduce system complexity and mission costs while optimizing onboard resources [9].

Laser communication systems are increasingly being adopted in space missions due to their high data rates, narrow beam divergence, and enhanced security compared to traditional radio frequency links [10]. Their adoption presents an opportunity to embed ranging capabilities directly

✉ Rashika Jain
r.jain-1@tudelft.nl

Dominic Dirkx
d.dirkx@tudelft.nl

Stefano Speretta
s.speretta@tudelft.nl

[1] Faculty of Aerospace Engineering, Delft University of Technology, Kluyerweg 1, Delft 2629 HS, The Netherlands

Published online: 12 February 2026

within laser communication terminals (LCTs). Unlike dedicated ranging systems, which are optimized solely for precise distance measurement, LCTs are primarily designed for data transfer and do not include time-tagging functionality by default. Ranging, however, fundamentally relies on an accurate and stable clock: the transmission and reception times of the signal must be tagged with sub-nanosecond precision to translate time of flight into distance. Any drift, jitter, or instability in the onboard clock directly propagates into range errors, which is why the clock becomes a critical component. Integrating ranging functionality into an LCT therefore requires the addition of precise timing electronics, careful signal processing, and synchronization mechanisms, as even small clock or electronic noise can directly degrade distance measurement precision. This dual-use approach can significantly reduce system complexity and SMaP requirements, but it also imposes stringent constraints on the onboard clock, detector, and time-tagging electronics to achieve reliable inter-satellite ranging performance. Within these subsystems, clock noise is often the dominant contributor to ranging errors [11, 12].

While laser communication systems and space-qualified clocks have been individually studied, limited work addresses how realistic clock-induced timing errors propagate through two-way inter-satellite laser ranging for small satellites. This paper addresses this gap by developing a methodology to unify clock noise specifications from datasheets in both frequency and time domains, generating timing noise spanning microseconds to hours. This framework is broadly applicable, enabling assessment of clock-induced errors across different formation geometries and operational scenarios. Using this approach, the study demonstrates the feasibility and limitations of high-precision two-way ranging via laser communication signal, and examines how clock errors affect orbit determination and the estimation of the gravitational parameter of a small body.

To assess the impact on mission performance, a test case involving a formation of two small satellites with inter-satellite ranging orbiting near-Earth asteroid 99942 Apophis is simulated [13, 14]. This concept follows the same line as already consolidated small-satellite demonstration missions such as DART–LICIACube [15], Comet Interceptor [16], HERA [17], and the RAMSES study [14], which explore coordinated multi-spacecraft operations for planetary defense and small-body science. Two orbital configurations for the formation are considered, coplanar and non-coplanar, to examine how relative satellite geometry affects the propagation of clock errors and the resulting ranging accuracy. Additionally, the study evaluates how clock-induced errors influence orbit determination and the estimation of the gravitational parameter of Apophis, critical for precise navigation and scientific measurements in asteroid missions.

By combining high-fidelity orbital propagation with detailed clock noise modeling, the analysis provides insights into the sensitivity of laser ranging measurements to clock stability over the entire range of integration periods. The results offer valuable guidance for designing satellite formation missions that integrate laser communication and ranging, highlighting scenarios where clock noise may limit ranging precision and science return.

The remainder of this paper is structured as follows. Section 2 describes the methodology for clock noise modeling and time series generation. Section 3 details the simulation framework, including the dynamical, observation, and estimation models. Section 4 presents the results, covering validation of the methodology, orbital dynamics, and the effects of clock noise on ranging and orbit estimation. Section 5 provides concluding remarks and outlines directions for future research. An overview of the complete workflow, from datasheet specifications to noise modeling, error generation, and orbit estimation, is shown in Fig. 1.

2 Methodology

In inter-satellite ranging, the distance between two satellites is determined by transmitting a signal from one satellite to the other and measuring the time of flight of the signal. The specific ranging technique depends on the signal type and the system architecture used for the measurement process [2]. In this work, asynchronous two-way ranging is implemented, where both satellites carry a transceiver and the signal is transmitted and received asynchronously. Regardless of the method, precise timing of the signal at both transmission and reception is essential, typically achieved using space-qualified atomic clocks or GPS-based timing

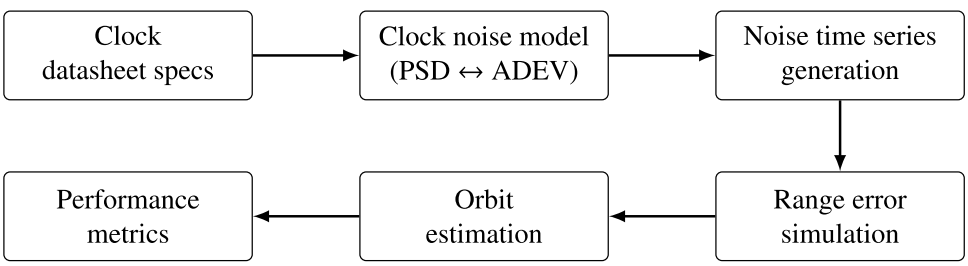

Fig. 1 Workflow from clock datasheet specifications to end-to-end orbit estimation and performance evaluation.

systems. While clock performance can be influenced by environmental factors such as thermal fluctuations or radiation, this study focuses specifically on the intrinsic stochastic instabilities of the clocks themselves, whose quantification is critical since they directly translate into errors in the measured range and, ultimately, mission performance.

This section presents the theoretical foundation of clock errors, reviews the state-of-the-art space-qualified clocks, and describes the methodology for converting datasheet clock specifications into range error models suitable for numerical simulations.

2.1 Clock error

The time error ($\Delta T(t)$) introduced by a clock can be modeled by Eq. (1), where T_0 is the initial synchronization offset, ($\Delta f/f$) represents the average initial frequency offset, D is the frequency drift or aging rate, and $\epsilon_c(t)$ captures the stochastic clock noise [18, Chapter 5]:

$$\Delta T(t) = T_0 + \left(\frac{\Delta f}{f}\right)t + \frac{1}{2}Dt^2 + \epsilon_c(t)\,. \tag{1}$$

The deterministic components T_0 and D are typically calibrated prior to deployment or corrected during operations. The term $\Delta f/f$ corresponds to the initial syntonization error, which includes the sum of the initial and average environmentally induced frequency offsets. Although its exact value depends on calibration uncertainties and the measurement process, it is generally treated as deterministic because it represents the average frequency offset established during calibration. In contrast, the stochastic term $\epsilon_c(t)$ accounts for the unpredictable fluctuations arising from intrinsic phase noise inherent in the clock signal and must be characterized statistically using measures such as power spectral density (PSD) or Allan deviation (ADEV).

Clock noise is commonly described in the frequency domain using the PSD of fractional frequency fluctuations, denoted by $S_y(f)$. It quantifies how the power of phase fluctuations is distributed across Fourier frequencies f relative to the carrier frequency f_c of the clock. It is commonly modeled as a sum of power-law components as given in Eq. (2) [18, Chapter 6]:

$$S_y(f) = \sum_{\alpha} h_\alpha f^\alpha\,, \tag{2}$$

where each coefficient h_α corresponds to a noise type characterized by spectral exponent α. Typical noise types and their spectral exponents are summarized in Table 1. The typical range of α spans from -4 to 2, capturing a variety of noise behaviors relevant to precision clocks. The PSD is particularly suited for characterizing short-term or high-frequency fluctuations, such as thermal noise, shot noise, or flicker noise, which occur on sub-second timescales.

Table 1 Classification of power-law noise types, with spectral exponent α and time-domain slope μ as used in PSD or AVAR analysis [18].

Noise type	α	μ
White phase modulation (WPM)	2	–
Flicker phase modulation (FPM)	1	–2
White frequency modulation (WFM)	0	–1
Flicker frequency modulation (FFM)	–1	0
Random walk frequency modulation (RWFM)	–2	1
Flicker walk frequency modulation (FWFM)	–3	2
Random run frequency modulation (RRFM)	–4	–

To characterize longer-term stability and correlated noise processes that may not be apparent in the frequency domain, the ADEV is employed in the time domain. Unlike standard deviation, which assumes stationary and uncorrelated noise, ADEV is specifically formulated to characterize time-dependent and correlated noise processes commonly found in precision oscillators. It is defined as the square root of the Allan variance (AVAR), which statistically measures how fractional frequency deviations y_i vary over averaging intervals of duration τ. The AVAR $\sigma_y^2(\tau)$ is expressed in Eq. (3) [18, Chapter 5]:

$$\sigma_y^2(\tau) = \frac{1}{2(N-1)}\sum_{i=1}^{N-1}\left(\bar{y}_{i+1} - \bar{y}_i\right)^2\,, \tag{3}$$

where $\bar{y}_i$ is the average fractional frequency over the i-th interval of duration τ and N is the number of such intervals in the dataset. Similar to PSD, AVAR can also be expressed as a sum of power-law noise components, as given in Eq. (4) [18, Chapter 5]:

$$\sigma_y^2(\tau) = \sum_{\mu} B_\mu \tau^\mu\,, \tag{4}$$

where the coefficients B_μ represent the contribution of a specific noise process, and the exponent μ characterizes its scaling with averaging time τ. The typical values of μ for different noise types are summarized in Table 1.

While PSD provides a complete spectral description of the clock noise, it is most accurate for short-term, high-frequency fluctuations and does not directly convey how these fluctuations accumulate over longer averaging times. Conversely, ADEV captures long-term stability and correlated noise for averaging times typically above 1 s, but is sensitive to very high-frequency fluctuations. Therefore, a comprehensive characterization of clock noise for inter-satellite ranging requires considering both representations:

PSD for high-frequency behavior and ADEV for long-term correlations.

2.2 Space-qualified clocks

Precision timing in satellites is achieved using high-performance atomic clocks. This section focuses on state-of-art clocks suitable for space missions, i.e., with lower SMaP constraints. These compact clocks are typically based on miniaturized quartz oscillators, chip-scale atomic clock (CSAC) technologies, or low-power rubidium atomic frequency standards (RAFS). An overview of a few representative space-qualified clocks meeting these constraints is provided in Table 2. These clocks were selected to span a broad range of size, mass, power consumption, and frequency stability, representative of current and emerging options for small satellite platforms. All of these devices are flight proven. This list is not exhaustive; the clocks are shown only as illustrative examples of different noise profiles and are not intended as a comprehensive review or mission-specific selection.

Clock datasheets provide the PSD $S_y(f)$ for $f > 1$Hz and ADEV $\sigma_y(\tau)$ for $\tau > 1$ s. Power-law exponents α and μ can be obtained from these datasheet values using Eq. (5):

$$\begin{aligned} \alpha_i &= \frac{\log S_y(f_i) - \log S_y(f_{i-1})}{\log f_i - \log f_{i-1}}, \\ \mu_i &= \frac{\log \sigma_y^2(\tau_i) - \log \sigma_y^2(\tau_{i-1})}{\log \tau_i - \log \tau_{i-1}}. \end{aligned} \tag{5}$$

Figure 2 shows the exponents associated with each clock, revealing that each device exhibits a unique combination of noise processes. It is apparent that α or μ values are not always integers. Therefore, although the integer power-law framework established in Sect. 2.1 effectively captures dominant noise contributions at different frequency offsets or averaging times, real-world clocks often exhibit simultaneous contributions from multiple noise processes, making simple integer-valued α or μ models insufficient for high-fidelity simulations. A recent study by [28] has demonstrated the benefit of generalizing these exponents to rational values, enabling more accurate replication of empirical clock noise, as reported in datasheets.

2.3 Time series of clock error

The output of a clock in ranging experiments is a time series representing timestamps of signal transmissions and receptions. To simulate realistic clock behavior, a clock noise time series is generated and added to the ideal (noise-free) timestamps, yielding noisy timestamps that approximate actual flight measurements.

A noise signal in time domain can be generated from a given PSD using the method developed by [29]. The fractional frequency PSD is first converted to time deviation PSD using Eq. (6):

$$S_x(f) = \frac{S_y(f)}{(2\pi f)^2}\,. \tag{6}$$

Random Fourier components are then drawn with amplitudes $\sqrt{S_x(f)/2}$ and independent Gaussian-distributed real and imaginary parts, while enforcing Hermitian symmetry to ensure a real time series. Finally, the inverse fast Fourier transform (IFFT) produces the clock time deviations $x(t)$:

$$x(t) = \mathrm{IFFT}\left\{ \sqrt{S_x(f)}\, e^{i\phi(f)} \right\}, \tag{7}$$

where $\phi(f)$ are random phases. This procedure yields a time series consistent with the target PSD, suitable for simulation of realistic clock noise. However, if the PSD given in datasheet is used, the phase noise will only represent high-frequency (short-term) noise, corresponding to timescales $\tau < 1$ s, such as white phase noise and flicker phase noise. But, two-way range measurements also involve long integration times due to propagation delays, retransmission delays, and signal integration, where low-frequency noise dominates. Therefore, to accurately quantify the timing errors introduced by a clock in a laser communication ranging system, its phase noise is modeled by combining high-frequency components derived from the PSD and low-frequency noise characterized by the ADEV as shown in Fig. 3.

To incorporate the ADEV components, datasheet ADEV values are converted to PSD using the methodology developed by [28], based on the standard relation between ADEV and PSD given in Eq. (8) [18]:

Table 2 State-of-the-art space-qualified clocks for small satellites.

Name	Material	Weight (kg)	Power (W)	Form factor	Flight heritage	References
Microchip CSAC SA45	Cesium	0.035	0.12	<1U	SPATIUM-I [19]	[20]
Safran MiniRAFS	Rubidium	0.45	10	~1U	–	[21]
Accubeat USO	Quartz crystal	2	6.5	$< 2U$	JUICE [22]	[23]
Safran RAFS	Rubidium	3.4	35	~3U	Galileo [24]	[25]
Excelitas RAFS	Rubidium	6.35	14	$> 3U$	GPS IIR [26]	[27]

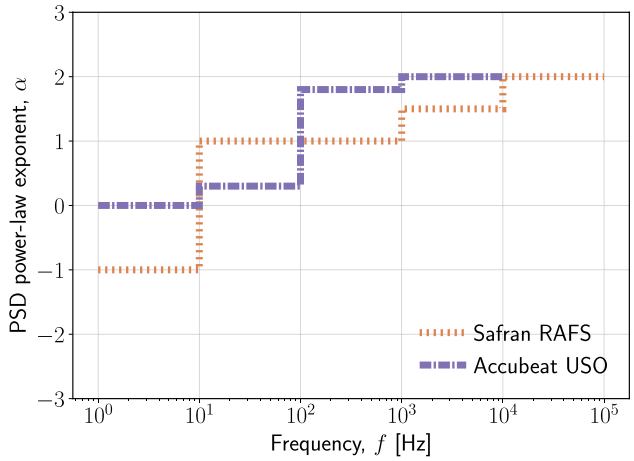

(a) PSD power-law exponent α versus offset frequency.

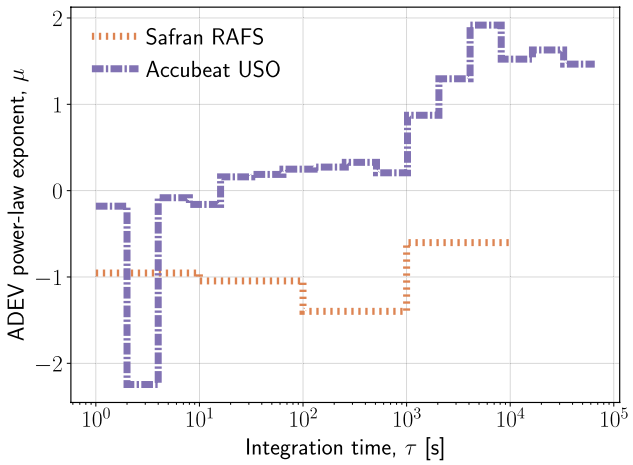

(b) ADEV power-law exponent μ versus integration time.

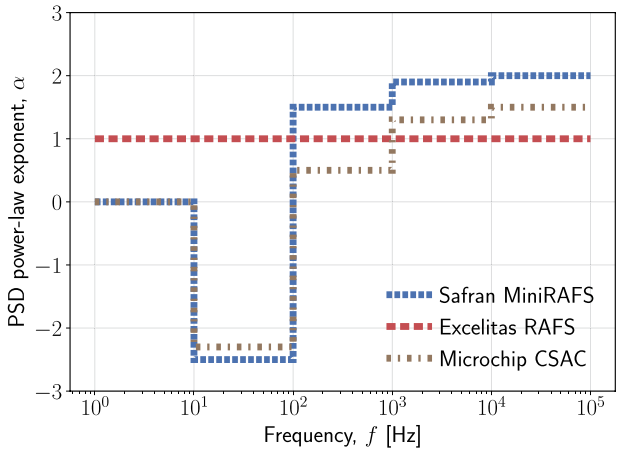

(c) PSD power-law exponent α versus offset frequency.

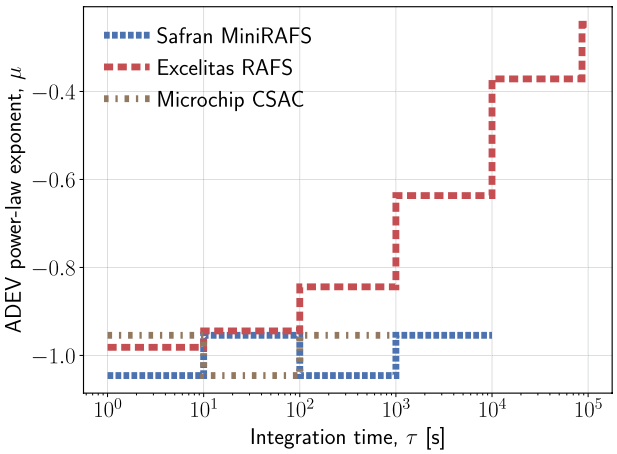

(d) ADEV power-law exponent μ versus integration time.

Fig. 2 Power-law spectral exponents α and temporal exponents μ as functions of offset frequency and integration times, respectively, characterizing stochastic noise in state-of-the-art space-qualified clocks.

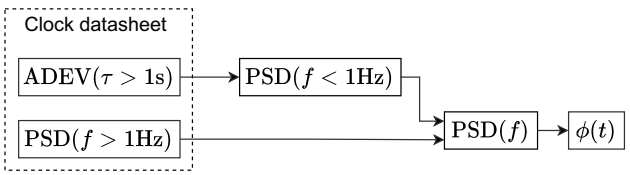

Fig. 3 Flowchart showing the generation of a unified time series capturing both short- and high-frequency clock noise.

$$\sigma_y^2(\tau) = 2\int_0^\infty h_\alpha f^\alpha \left[\frac{\sin^4(\pi\tau f)}{(\pi\tau f)^2}\right] df\,. \tag{8}$$

The methodology draws a direct correspondence between the power laws in the frequency and time domains. By representing the ADEV given in datasheet using Eq. (4), values of B_i and μ_i can be obtained for every i-th pair of $(\tau, \sigma_y^2(\tau))$, and the corresponding $S_y(f)$ values are obtained from Eqs. (2), (9), (10) [28].

$$\begin{aligned} &\alpha_i = -\mu_{n-i+1} - 1; \qquad h_i = \frac{B_{n-i+1}\pi^{\alpha_i+1}}{2I_i^\infty}; \\ &I_i^\infty = \int_0^\infty \frac{\sin^4 z}{z^{2-\alpha_i}}\, dz; \qquad i = 1, \ldots, n \end{aligned} \tag{9}$$

$$f_i = \frac{1}{\pi}\left(\frac{B_{n-i+1}}{B_{n-i}}\frac{I_{i+1}^\infty}{I_i^\infty}\right)^{\frac{1}{\alpha_{i+1}-\alpha_i}}, \qquad i = 1, \ldots, n-1. \tag{10}$$

It should be noted that these equations are only valid where the integral in Eq. (8) converges, i.e., for spectral indices $-3 < \alpha < 1$ (see Appendix A for justification). From Eq. (9), the corresponding time-domain exponents should satisfy $-2 < \mu < 2$, which is consistent with the values observed in Fig. 2a and d for all clocks. Hence, the methodology

described above to convert ADEV to PSD is applicable to the clocks considered in this study.

By combining the high-frequency PSD from datasheets and low-frequency PSD derived from Eqs. 10 and 9, a complete PSD profile is obtained. This profile is used to generate time deviation series $x(t)$ based on Eqs. 6 and 7 [29]. To reduce computational load and memory requirements, two separate time series are generated: a coarse time series $x_{\text{coarse}}(t)$ spanning the entire mission duration to capture low-frequency, long-term drift, and a fine time series $x_{\text{fine}}(t)$ over each measurement window to capture high-frequency, short-term fluctuations. The coarse series is interpolated within each measurement window to match the timestep of the fine series (t_m), ensuring consistent representation of both low- and high-frequency noise. Depending on the mission duration and chosen timesteps, typical phase error series consist of up to points, illustrating the computational scale of the simulation. At each timestamp within a measurement window m, the total timing error $\epsilon_{\alpha,c}^{(m)}$ introduced by the onboard clock of satellite α is defined by Eq. (11):

$$\begin{aligned}\epsilon_{\alpha,c}^{(m)}[n] = &\underbrace{\text{interp}\left(x_{\text{coarse}}\,[0 : N_{\text{coarse}} - 1],\, t_n\right)}_{\text{coarse time series over full mission, interpolated}} \\ &+ \underbrace{x_{\text{fine}}^{(m)}[n]}_{\text{fine series for measurement window } m}; \\ n = 0, 1, \ldots, N_{\text{fine}} - 1; \quad &N_{\text{fine}} = \frac{T_{\text{window}}}{t_m}; \\ t_n = n\, t_m; \quad &N_{\text{coarse}} = \frac{T_{\text{total}}}{\Delta t_{\text{coarse}}},\end{aligned} \tag{11}$$

where N_{coarse} is the number of coarse time steps over the full mission, T_{total} is the total mission duration, Δt_{coarse} is the coarse time step, t_m is the measurement step, T_{window} is the duration of a single measurement window, and N_{fine} is the number of fine time steps within a measurement window. The complete clock error sequence $\epsilon_{\alpha,c}$ over the mission is then obtained by assembling the per-window realizations $\epsilon_{\alpha,c}^{(m)}$ in chronological order:

$$\epsilon_{\alpha,c} = \left[\epsilon_{\alpha,c}^{(0)}, \epsilon_{\alpha,c}^{(1)}, \ldots, \epsilon_{\alpha,c}^{(M-1)}\right], \tag{12}$$

where $M = T_{\text{total}}/T_{\text{window}}$ is the number of measurement windows. Thus, $\epsilon_{\alpha,c}$ is not generated as a single realization over the full mission, but rather as a sequence of window-wise realizations stitched together to span the mission timeline.

The resulting time deviations from Eq. (12) are then added to the simulated time-of-flight measurements to produce noisy range measurements. The sampling interval and total duration of the generated clock error series are chosen to match the specific observation model and mission scenario, ensuring that the simulated noise aligns with the timing resolution and integration windows of the ranging system.

It should be noted that the fast Fourier transform (FFT)-based approach used here correctly reproduces the target PSD in the generated time series, but can underestimate the time-domain variance of flicker frequency noise ($S_y(f) \propto 1/f^3$) in finite-length samples. This limitation arises from the intrinsic non-stationarity of $1/f$ processes and from FFT windowing effects that suppress very low-frequency components [30]. Consequently, while the low-frequency PSD derived from ADEV remains theoretically valid at $\alpha = -3$, individual realizations may exhibit smaller phase drifts than predicted by infinite-time analytical models. This bias is not explicitly corrected in the current simulations, because the study focuses on capturing general trends in orbit estimation errors due to clock noise rather than precise long-term phase deviations. Moreover, all noise amplitudes are anchored to measured ADEV values from datasheets, ensuring that the relative contribution of flicker FM to overall orbit estimation errors remains representative. For future studies or for clocks strongly dominated by flicker FM, a corrected FFT-based synthesis with improved low-frequency weighting, such as that proposed by [30], is recommended.

Moreover, the methodology relies on manufacturer-provided ADEV and PSD data, which may deviate from the actual clock performance in the space environment due to unmodeled effects such as temperature variations, radiation, or aging. This introduces uncertainty in absolute noise levels, though relative performance trends between clocks remain robust. Flight implementation of any clock should therefore be validated through extended laboratory characterization or in-flight calibration. Nevertheless, the methodology is fully general and remains applicable if datasheet values are replaced with experimentally derived f-PSD and τ-ADEV measurements.

3 Simulation setup

This section describes the simulation setup developed to evaluate the impact of onboard clock errors on inter-satellite LCT ranging and orbit determination performance. The mission scenario is loosely based on ESA's RAMSES concept [14, 31] and is used here as a representative test case to demonstrate the methodology rather than to reproduce the original mission in detail. While RAMSES involves a mothercraft and one or more small satellites, the present study focuses on a simplified configuration of two satellites operating around the near-Earth asteroid 99942 Apophis. This abstraction allows the analysis to remain method driven while maintaining a realistic dynamical and operational context.

In the modeled scenario, two CubeSats (C1 and C2) fly in formation around Apophis, approximately 2 months prior

to its close Earth flyby on April 13, 2029. Both spacecraft are equipped with X-band transceivers for two-way Doppler tracking to Earth and with LCT to establish a bidirectional optical inter-satellite link (ISL). Each satellite carries an independent onboard clock, which is used to timestamp transmitted and received optical signals for inter-satellite ranging. The combined radiometric and optical measurements enhance both absolute and relative orbit determination, improving navigation accuracy and enabling more robust estimation of the gravity field of the asteroid. Beyond its scientific role, the ISL also provides high-rate payload data transfer, inter-satellite time synchronization, and the possibility of performing autonomous coordinated tasks, particularly during periods of reduced visibility from Earth.

The subsequent subsections detail the dynamical model, observation model and realization, inter-satellite communication link specifications, and estimation methodology, with the objective of quantifying the impact of onboard clock errors on ranging precision and orbit determination.

3.1 Dynamical model

The dynamical model describes the orbital motion of two satellites around the near-Earth asteroid 99942 Apophis, considering two distinct relative formations: coplanar and non-coplanar. In the *coplanar* configuration, the satellites are separated primarily along their orbital path (tangent to the orbit), resulting in a leading–trailing formation. In the *non-coplanar* configuration, the separation is mainly perpendicular to the orbital plane, creating an out-of-plane offset between the satellites. These two cases represent different geometric sensitivities for inter-satellite ranging and are used to assess the robustness of orbit determination, both for precise navigation around the asteroid and for the estimation of gravitational parameter of Apophis.

The initial conditions for satellites C1 and C2 in both configurations are listed in Table 3. These conditions are based on the orbital elements reported by [32], with parameters adjusted to generate sufficient variation in relative geometry and ensure observability of the inter-satellite measurements.

Table 3 Initial orbital parameters for satellites C1 and C2 for coplanar and non-coplanar orbit configurations. C1 has identical initial conditions in both configurations.

Orbital parameters	C1	C2 coplanar	C2 non-coplanar
Periapsis	500 m	500 m	700 m
Eccentricity	0.01	0.01	0.05
Inclination	75 °	75 °	85 °
Argument of periapsis	90 °	90 °	90 °
RAAN	45 °	45 °	55 °
True anomaly	90 °	180 °	270 °

In both scenarios, C1 maintains the same initial conditions, while altitude, inclination, and true anomaly of C2 are adjusted to realize the desired relative geometry. The initial inter-satellite separation is 1 km in the coplanar case and 1.6 km in the non-coplanar case. The relative distance evolves over time due to orbital dynamics, which are propagated over an 8-day period to generate true time-of-flight values for inter-satellite range measurements.

The gravitational field of Apophis is represented using a spherical harmonics model based on its estimated mass ($\approx 5.31 \times 10^{10}$ kg). The associated coefficients C_{lm} and S_{lm} (l: degree, m: order) are taken from [32]. For the current analysis, the expansion is truncated at degree and order 4 ($l, m \in [0, 4]$), which provides computational efficiency and is adequate at the radial distances of 600–1000 m considered here. However, due to the highly irregular shape of Apophis, this representation may not resolve fine-scale variations in the gravitational field near the surface; for close-proximity operations or landing scenarios, the use of higher-degree gravity representations, such as polyhedral models, is recommended [32]. The rotational state of the asteroid is also included in the model, with the initial pole orientation set to a right ascension of 250 ° and a declination of 75 °, ensuring that the gravitational potential accounts for both mass distribution and rotation [33, 34].

Additional perturbations are included as follows: the Sun and Moon are modeled as point masses; gravitational field of Earth is represented with spherical harmonics up to degree and order 2; and solar radiation pressure is incorporated through a cannonball model parameterized by the satellite surface area, reflectivity, and mass.

The true relative position between C1 and C2 is computed at each time step to derive the true time of flight (t_{TOF}), which forms the basis of inter-satellite range measurements described in the following section.

3.2 Observation model

This section describes the mathematical formulation of the measurements implemented in the orbit estimation framework, focusing on two primary types: inter-satellite LCT-based two-way time of flight (TOF) ranging via the optical ISL, and Doppler tracking to Earth using a typical deep space network (DSN) radio tracking system. These measurements are complementary: Doppler data provide absolute velocity information relative to Earth, while the ISL offers high-precision relative range between the two satellites.

3.2.1 Inter-satellite range observable

For the ISL, the cumulative two-way range observable, $h_{\text{2-range}}$, is computed as the sum of two one-way range

measurements along the signal path from transmitter to receiver and back:

$$h_{\text{2-range}}(t_T) = h_{\text{1-range}}(t_T, t_{R1}) + h_{\text{1-range}}(t_{T2}, t_{R2}), \tag{13}$$

where t_T is the transmission time from the first spacecraft, t_{T2} is the transmission time from the second spacecraft, t_{R1} is the reception time at the second spacecraft, and t_{R2} is the reception time at the first spacecraft. $h_{\text{1-range}}$ denotes the one-way range observable given as:

$$h_{\text{1-range}}(t_T, t_R) = \left\| \mathbf{r}_R(t_R) - \mathbf{r}_T(t_T) \right\| + \Delta s, \tag{14}$$

where $\mathbf{r}_R(t_R)$ and $\mathbf{r}_T(t_T)$ are the position vectors of the receiver and transmitter at the reception and transmission times t_R and t_T, respectively, and Δs represents any additional known signal path corrections such as relativistic or deterministic delays. For the short inter-satellite distances considered here, Δs is negligible, so the true two-way time of flight t_{TOF} between satellites C1 and C2 is effectively determined by the geometric separation and is given by:

$$t_{\text{TOF}}(t_T) = \frac{h_{\text{2-range}}(t_T)}{c}. \tag{15}$$

This idealized formulation does not include noise sources, which are introduced in the observation realization.

For clarity, in this paper the terminology "one-way" refers to a single signal path, while "two-way" refers to the sum of the uplink and downlink paths, i.e., the total round-trip range or time of flight between the satellites.

3.2.2 Doppler observable

The Doppler measurements used in this study correspond to the two-way, time-averaged Doppler formulation computed from the difference of two two-way range measurements, referenced to the receiver time, divided by the integration interval Δt:

$$h_{2-\bar{\text{D}}\text{opp}}(t) = \frac{h_{\text{2-range}}(t_R = t + \Delta t) - h_{\text{2-range}}(t_R = t)}{\Delta t}, \tag{16}$$

where $h_{\text{2-range}}$ denotes the two-way range observable and Δt is the Doppler integration time. In practice, this corresponds to averaging the instantaneous Doppler over the integration interval, consistent with the operation of DSN tracking systems.

3.3 Observation realization

This section describes how the true measurements are generated from the spacecraft trajectories. The realization accounts for the ISL performance, communication protocol, and operational constraints. All measurements are considered noise free.

3.3.1 Inter-satellite range realization

The inter-satellite range measurements are generated using data transmitted by the LCT, so their realization depends on the characteristics of the communication link. In particular, the feasible measurement cadence—i.e., how frequently range observations can be obtained—is determined by the performance of the optical link. The received power, achievable bit rate, and frame duration collectively dictate the maximum rate at which measurements can be generated.

The LCTs used are similar to those demonstrated on the CLICK mission, with specifications listed in Table 4 [12]. Communication employs on–off keying (OOK) modulation with direct detection via an Avalanche photodetector (APD) and the ESA Specification for Terabit/sec Optical Links (ESTOL) protocol with a frame size of 9504 bits (Table 5) [35]. Each frame contains a mission-specific identifier, which is time-tagged at both transmission and reception on C1 and C2. Post-processing of these identifiers yields the realized two-way inter-satellite range measurements.

The cadence of the inter-satellite range measurement is fundamentally constrained by the bit rate of the communication link. The maximum achievable bit rate of the inter-satellite optical link is fundamentally determined by the available bandwidth of the hardware and the spectral efficiency of the chosen modulation scheme. For a given bandwidth B and modulation efficiency η (bits per second per Hz), the theoretical maximum bit rate is:

$$R_{\text{max}} = B \cdot \eta. \tag{17}$$

The modulation efficiency depends on the chosen modulation format (equal to 1 for OOK in this study), while the bandwidth is limited by the transmitter and receiver hardware. In practice, coding schemes reduce the information rate but improve reliability, effectively modifying the usable spectral efficiency.

Once the target bit rate is defined, a link budget analysis is performed to ensure that the optical link can support this rate under worst-case conditions. The transmitted optical signal experiences attenuation due to free-space propagation, optical losses, pointing errors, and electronic inefficiencies, all of which reduce the received power. The instantaneous received power P_r can be estimated using the Friis transmission equation [36]:

$$P_r = P_t \cdot G_t \cdot \mu_t \cdot L_{fs} \cdot L_p \cdot G_r \cdot \mu_r, \tag{18}$$

where P_t is the transmit power, G_t and G_r are the transmitter and receiver gains, μ_t and μ_r are the optical losses, L_{fs} is the

Table 4 LCT specifications for the ISL, including laser, transmitter, receiver, and APD parameters [12].

Laser parameters		
λ	Wavelength	1550 nm
P_t	Transmit power	200 mW
Transmitter parameters		
D_t	Aperture diameter	1.3 cm
$\theta_{1/2}$	Half divergence	75 µrad
θ_p	Pointing accuracy	-5 µrad
μ_t	Optical loss	0.7
T_f	Frame duration	1 µs
Receiver parameters		
D_r	Aperture diameter	1.3 cm
α_r	Truncation ratio	0
μ_r	Optical loss	0.7
$\Delta\lambda$	Bandpass filter width	0.2 nm
FOV	Field-of-view	1 mrad
APD parameters		
η	Quantum efficiency	0.8
G	Gain	10
F	Excess noise factor	3.5
B	Filter bandwidth	500 MHz
σ_d	Jitter	240 ps
I_{dc}	Unmultiplied dark current	2.5 nA
I_{amp}	Amplifier current	2.1 pA

Table 5 Frame composition of the ESTOL protocol, showing field names, descriptions, and sizes in bits [35].

Field	Description	Size (bits)
Frame identifier	Unique frame sync marker	64
Header	Metadata	960
Payload	Data	8448
Error correction	CRC or FEC codes	32
Total		9504

free-space path loss, L_p is the pointing loss. The individual terms are given by:

$$G_t = \frac{8}{\theta_{1/2}^2}, \quad G_r = \left(\frac{\pi D_r}{\lambda}\right)^2 \cdot (1-\alpha_r^2),$$
$$L_{fs} = \left(\frac{\lambda}{4\pi d}\right)^2, \quad L_p = \exp\left\{-2\left(\frac{\theta_p}{\theta_{1/2}}\right)^2\right\}, \tag{19}$$

where d is the inter-satellite distance. In addition to attenuation, the received signal is affected by noise from the detector and electronics. This noise is accounted for in the noise budget (Appendix B) and combined with the received power P_r to compute the effective signal-to-noise ratio (SNR).

For a successful link, the received power must exceed a minimum threshold defined by the target bit-error rate (BER), i.e., the number of possible error bits that can be received on a certain link. Encoding schemes are used to minimize BER and increase redundancy, improving the likelihood of correct signal detection. For a given modulation and coding scheme, the required SNR and power to meet a target BER is given by Eqs. 21 and 20:

$$\mathrm{SNR}_{req} = \frac{8}{f} \cdot \left[\mathrm{erfc}^{-1}(2 \cdot \mathrm{BER})\right]^2 - \text{Coding Gain} \tag{20}$$

$$P_{req}^{(2)} \geq \frac{\sigma_n}{G \cdot R_d} \cdot \mathrm{SNR}_{req}\,, \tag{21}$$

where σ_n is the total noise power, G is the detector gain, R_d is the detector responsivity, and f is the modulation factor (equal to 1 for OOK modulation in this study). The coding gain accounts for the improvement due to error-correcting codes. In this study, a conservative coding gain of 1 dB is assumed.

The link is typically designed for the worst-case scenario, corresponding to the maximum inter-satellite separation $d_{\max}$. The received power at this distance is used to compute the noise power σ_n, and the link margin is defined as the difference between received and required power. A positive link margin indicates that the link can be reliably established, while a negative link margin requires either reducing the bit rate or increasing the transmitted power to maintain communication.

Finally, the communication system is designed to satisfy both the mission-required bit rate and link feasibility. From the bit rate and the frame structure of the communication protocol (here, ESTOL), the frame duration t_f and the effective data rate can be calculated using Eqs. 22 and 23:

$$t_f = 9504/R \text{ s}, \tag{22}$$

$$\begin{aligned}\text{Data rate} &= \text{Frame rate} \times \text{Payload bits per frame} \\ &= 8448/t_f\end{aligned} \tag{23}$$

To generate inter-satellite range measurements, each communication frame is time-tagged at its start, which directly determines the temporal resolution of the measurements. Figure 4 illustrates the timestamping scheme for two consecutive measurements in a single observation pass. The time-tags obtained from the transmitted and received frames are post-processed to compute the measured two-way inter-satellite range for the n-th measurement set, ρ_n, as:

$$\rho_n(t_{n,1}) = \frac{c}{2}\left[(t'_{n,2} - t_{n,1}) + (t_{n,4} - t'_{n,3})\right], \tag{24}$$

where $t_{n,i}$ and $t'_{n,i}$ denote the times recorded by the clocks on C1 and C2, respectively, converted to a common time scale.

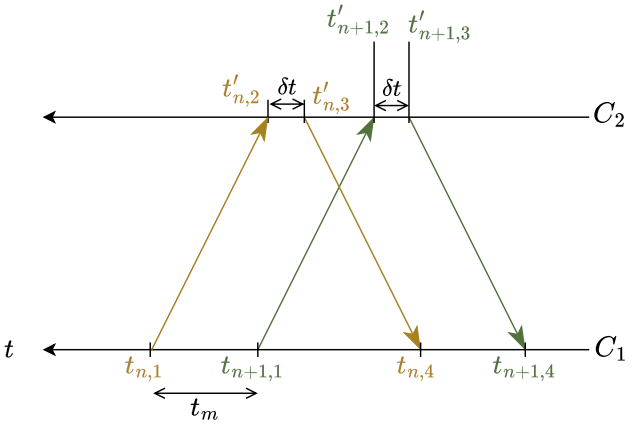

Fig. 4 Timestamps in two-way range measurements in a single observation pass. Variables t and t' denote the times recorded by the clocks on C1 and C2, respectively; δt represents the transmission offset, reflecting the asynchronous timing between reception and the subsequent transmission at the second satellite; and t_m indicates the step size between consecutive measurements.

These time-tags mimic the behavior of a real system clock and are related by the following equations:

$$t'_{n,2} = t_{n,1} + t_{\text{TOF}}(t_{n,1}), \tag{25}$$

$$t'_{n,3} = t'_{n,2} + \delta t, \tag{26}$$

$$t_{n,4} = t'_{n,3} + t_{\text{TOF}}(t'_{n,3}), \tag{27}$$

$$t_{n+1,1} = t_{n,1} + t_m, \tag{28}$$

where δt, hereafter referred to as the transmission offset, represents the temporal difference between the received and transmitted frames at the second satellite. This offset captures the asynchronous nature of the inter-satellite measurements and may result from observation scheduling, protocol timing constraints, or minor differences in the spacecraft clocks.

These time tags are only used to generate a noise time series that mimics realistic measurement timing. In the simulations, range measurements are taken with step size t_m determined by the signal frame duration (Eq. (22)). Consecutive observation passes are separated by a waiting interval $t_{\text{wait}} = 10$ min, with each pass consisting of $N = 1000$ individual range measurements. While a communication signal may contain many more frames, this number of measurements per pass is sufficient to capture the temporal evolution of the inter-satellite range and the effect of clock noise, while keeping computational cost reasonable. The choice of N is arbitrary; using fewer or more measurements would not qualitatively affect the resulting range error, provided the temporal sampling adequately resolves the dynamics of interest.

In summary, the temporal resolution of the inter-satellite range measurements is governed by the frame duration and the onboard clock. Because measurement timing is governed by discrete clock ticks, the achievable measurement frequency is typically constrained to integer multiples or divisors of the clock frequency. Link analysis ensures that the selected bit rate and frame rate remain consistent with the physical and operational limitations of the optical link and the onboard clock. Although higher measurement frequencies are attainable through advanced techniques such as phase-locked loops (PLL), the current time-tagging approach offers a realistic and tractable representation of the measurement process for simulation purposes.

3.3.2 Doppler realization

Two-way averaged Doppler measurements are computed from the difference of consecutive two-way range measurements over the Doppler integration interval. An integration

time of $\Delta t = 60$s is used, and Doppler measurements to both satellites are acquired from DSN tracking stations for 1 h, twice per day [14].

3.4 Measurement errors

The observables described in the previous section are initially generated as noise-free quantities from the propagated spacecraft trajectories. To realistically emulate system performance, measurement errors must be included. These errors represent hardware imperfections, signal processing limitations, and stochastic noise sources affecting both the ISL and ground-based Doppler tracking. The following subsections describe the error models applied to each measurement type.

3.4.1 Inter-satellite range errors

For the ISL, the dominant error sources are the stochastic timing fluctuations of the onboard atomic clocks, detector jitter, and time-tagging uncertainty. The measured two-way range ρ_{meas} is modeled as:

$$\rho_{\text{meas}} = \frac{c}{2}\left(t_{\text{TOF}} + \epsilon_{C1} + \epsilon_{C2}\right), \tag{29}$$

where ϵ_{C1} and ϵ_{C2} denote the total errors at satellites C1 and C2, respectively, and t_{TOF} is the true two-way TOF computed from the relative positions of the satellites obtained from the propagated orbits using Eq. (15).

Clock errors are modeled as a band-limited Gaussian random process, characterized by the PSD and ADEV specified in the clock datasheet (see Sect. 2.3). These errors capture both long-term drift and short-term fluctuations. Since each satellite carries an independent onboard clock, separate noise realizations are generated for C1 and C2. The transmission offset δt between the received and transmitted frames effectively sets the integration interval over which the two-way clock errors accumulate, thereby influencing the magnitude of the resulting range error.

Detector jitter (ϵ_d) and time-tagging errors (ϵ_t) are modeled as Gaussian processes. The standard deviation for detector jitter is set to 240 ps, consistent with state-of-the-art spaceborne APD detectors [12, 37]. For time-tagging errors, a standard deviation of 200 ps is assumed [5, 12, 38, 39]. Laboratory telemetry ranging tests performed using the Frontier Radio achieved a time-of-arrival precision of 2–3.5 ns at kilobit-per-second data rates [5]. Given that laser communication operates at gigabit-per-second rates, roughly five orders of magnitude higher, the assumed 200 ps is realistic for high-speed LCT. The dominant contributions to ϵ_d arise from the intrinsic response time of the avalanche photodiode and its readout electronics, whereas ϵ_t primarily reflects quantization and processing uncertainties within the time-tagging circuitry.

The total range error ϵ_α at any satellite α is therefore given using Eq. (30):

$$\epsilon_\alpha = \epsilon_{\alpha,c} + \epsilon_{\alpha,t} + \epsilon_{\alpha,d}\,,\ \alpha \in (C1, C2) \tag{30}$$

$$\epsilon_\alpha = \epsilon_{\alpha,c} + \mathcal{N}\{0, (2\cdot 10^{-10})^2\} + \mathcal{N}\{0, (2.4\cdot 10^{-10})^2\}, \tag{31}$$

where $\epsilon_{\alpha,c}$ is a segmented clock noise series, obtained by assembling independent realizations for each measurement window according to Eq. (12).

3.4.2 Doppler errors

For Doppler tracking, receiver and processing noise are the primary error sources. These are represented as Gaussian perturbations added to each Doppler measurement:

$$\epsilon_{\text{Dopp}} \sim \mathcal{N}\{0, \sigma^2_{\text{Dopp}}\}\,, \tag{32}$$

where σ_{Dopp} is the standard deviation of the Doppler noise ϵ_{Dopp}. In this study, a conservative value of $\sigma_{\text{Dopp}} = 1$ mm/s is adopted to reflect typical receiver performance [40]. The observed Doppler is then given by Eq. (33):

$$\dot{\rho}_{\text{meas}} = h_{2-\bar{\text{D}}\text{opp}} + \epsilon_{\text{Dopp}}\,. \tag{33}$$

3.5 Estimation model

The previous subsections defined the measurement process. The inter-satellite range and Doppler measurements contain information about the relative and absolute motion of the satellites, but they are corrupted by measurement errors. By generating these measurements with associated noise realizations, the framework produces a set of synthetic observables that realistically emulate the performance of the measurement system. Estimating the initial state vectors of the satellites from these observables enables assessment of how measurement errors propagate into orbit determination and allows evaluation of the achievable precision of the mission tracking system.

For this purpose, a batch least-squares algorithm [41] is employed to retrieve the initial state vectors of satellites C1 and C2 as well as the gravitational parameter μ of Apophis, forming the set of estimated parameters $\mathbf{q}$ as:

$$\mathbf{q} = [\mathbf{X}_{C1},\ \mathbf{X}_{C2},\ \mu]^T\,,$$
$$\text{where } \mathbf{X}_\alpha = [x_\alpha, y_\alpha, z_\alpha, \dot{x}_\alpha, \dot{y}_\alpha, \dot{z}_\alpha]^T\,,\ \text{for } \alpha \in \{\text{C1}, \text{C2}\}. \tag{34}$$

The estimator processes two types of observables. Firstly, two-way inter-satellite range measurements, generated as described in Sect. 3.3.1 and affected by clock-induced errors,

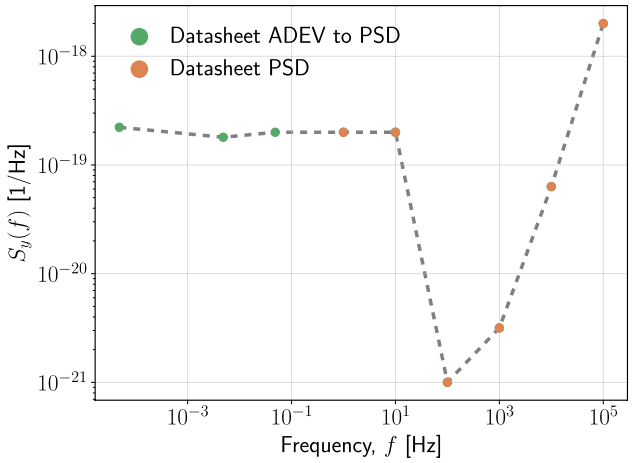

Fig. 5 PSD as a function of frequency for Microchip CSAC. The PSD values below 1 Hz are obtained by conversion from datasheet ADEV, the values above 1 Hz are directly from the datasheet [20].

detector jitter, and time-tagging uncertainties. These measurements provide high-precision information on the relative separation between the satellites but do not fully constrain the absolute state in the Apophis-centered inertial frame. Secondly, two-way Doppler measurements, obtained from Earth-based tracking, providing the line-of-sight velocity of each satellite relative to the reference frame. The latter are primarily included to ensure observability (ability to uniquely determine the state from the available measurements) of the absolute states. These measurements form the set of modeled observations $\mathbf{h}$.

The design matrix $\mathbf{H} = \partial\mathbf{h}/\partial\mathbf{q}$ is formed by computing the partial derivatives of each observable with respect to the estimated parameters. $\mathbf{H}$ matrix quantifies how small changes in the parameters affect the predicted measurements. The covariance matrix, $\mathbf{K}$, is computed from Eq. (35),

$$\mathbf{K} = \left(\mathbf{H}^{\mathrm{T}}\mathbf{W}\mathbf{H} + \mathbf{K_0}\right)^{-1}, \tag{35}$$

where $\mathbf{W}$ is the weight matrix of the observations, and $\mathbf{K_0}$ is the a priori covariance matrix. The a priori uncertainties are set to 15 m in position and 15 mm/s in velocity for both satellites, providing a baseline constraint for the initial parameter estimates.

The weight matrix is typically set as diagonal with entries corresponding to the inverse variance of each measurement, however, since two types of observables with different units and noise characteristics are added to the estimator, measurement weights are defined to balance their contributions [42]:

$$\mathbf{W} = \begin{cases} \sigma_{\text{range}}^{-2}, & \text{for range measurements} \\ \sigma_{\text{Dopp}}^{-2} \cdot \dfrac{N_r}{N_d}, & \text{for Doppler measurements} \end{cases}, \tag{36}$$

where N_r and N_d are the number of range and Doppler measurements, respectively, σ_{range} is the standard deviation of the total range error (Eq. (30)), and σ_{Dopp} is the standard deviation of the Doppler measurement noise. The scaling factor N_r/N_d ensures that the relative contribution of each measurement type to the estimation is proportional to the number of available observations. Without this normalization, the large imbalance in the number of range and Doppler data points leads to an ill-conditioned normal matrix and poor numerical stability of the estimator.

The parameter update $\Delta\mathbf{q}$ is computed iteratively using:

$$\Delta\mathbf{q} = \mathbf{K}\left(\mathbf{H}^{\mathrm{T}}\mathbf{W}\Delta\mathbf{h}\right), \tag{37}$$

where $\Delta\mathbf{h}$ is the residual vector between the modeled and measured observations. Iterations continue until the relative change in the residual $\Delta\mathbf{h}$ in consecutive iterations is below a defined tolerance.

The estimated parameters obtained after convergence are then compared with the true initial states and the true value of μ from the simulation, allowing the computation of true errors in position, velocity, and gravitational parameter. These true errors provide a direct measure of the accuracy of the estimation under the influence of the modeled measurement noise.

3.6 Simulation overview and objectives

The simulation framework generates synthetic inter-satellite range and Earth-based Doppler measurements to perform orbit determination for two satellites in the Apophis-centered inertial frame. Inter-satellite range measurements, affected by stochastic clock noise, detector jitter, and time-tagging uncertainties, and Doppler measurements are used as inputs to a batch least-squares estimator. This retrieves the initial state vectors of satellites C1 and C2 and the gravitational parameter μ of Apophis, assessing how measurement errors propagate into orbit determination accuracy.

The primary objective of the simulations is to study the impact of clock noise on inter-satellite ranging and, consequently, on orbit determination. To this end, the transmission offset, δt, is systematically varied to capture the effect of different integration times over which two-way clock errors accumulate, while all other noise sources remain fixed. For each δt, 1000 Monte Carlo runs are performed to obtain statistically robust estimates of position, velocity, and gravitational parameter errors. Clock noise profiles for both satellites are independently generated for each run, producing

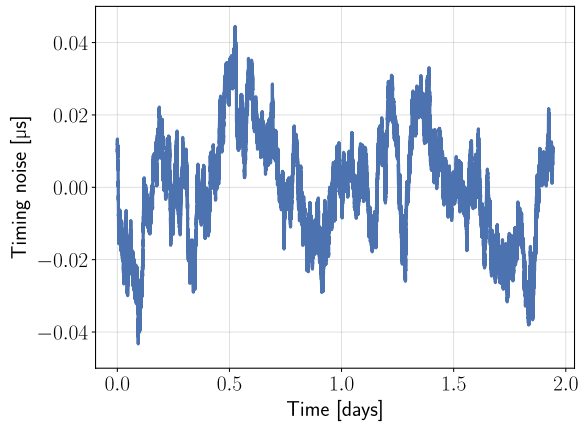

(a) Coarse clock noise over the mission duration of 2 days, generated with a sampling interval of 0.01 s. The vertical axis shows noise amplitude in μs.

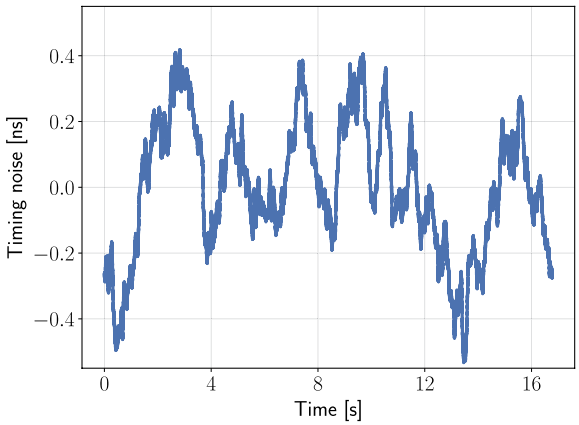

(b) Fine clock noise for an observation pass of 16 s, generated with a sampling interval of 1 μs. The vertical axis shows noise amplitude in ns.

Fig. 6 Absolute clock noise over the total mission duration (coarse) and over individual observation passes (fine).

unique two-way range noise (refer to Sect. 2.3). In contrast, 1000 independent Doppler noise profiles are generated once and reused across all δt runs, so that the i-th run for any δt uses the same i-th Doppler noise profile. This setup ensures that variations in the estimated states between different δt runs are solely due to clock noise.

A baseline scenario using only Doppler measurements, excluding inter-satellite range data, isolates the influence of inter-satellite clock errors from other measurement noise. Estimation performance is quantified using the root mean square error (RMSE) of true errors over 1000 runs. Convergence of the Monte Carlo simulations was assessed by tracking the RMSE as the number of realizations increased. The RMSE was considered converged once successive values changed by less than 1%. Under this criterion, convergence was reached after approximately 500 realizations for short transmission offsets and around 800 realizations for longer offsets. To ensure uniformity and enable consistent comparison across all scenarios, 1000 realizations were used in all cases. Overall, the framework provides a systematic evaluation of the precision and robustness of LCT-based inter-satellite ranging in the dynamical environment of Apophis, explicitly accounting for stochastic clock noise. All mission propagation and estimation simulations were carried out using the open-source TU Delft Astrodynamics Toolbox (Tudat)[1] [43].

[1] Documentation: https://tudat-space.readthedocs.io, Source code: https://github.com/tudat-team/tudat-bundle

4 Results

This section presents the results of the analysis described in Sect. 3.6. Section 4.1 presents the validation of the algorithm described in Sect. 2.3 to generate clock noise from datasheet. Section 4.2 demonstrates the satellite orbits used in the dynamical model for estimation setup and Sect. 4.3 gives the specifications of the communication link obtained from the link analysis done in Sect. 3.3.1. Finally Sect. 4.4 presents the results of the Monte Carlo simulations, with focus on the impact of clock noise on two-way range and the true errors in satellite states and gravitational parameter.

4.1 Validation of clock noise generation

This subsection presents and validates the general noise-generation methodology using the Microchip CSAC clock before applying it to any specific mission scenario. Following the approach detailed in Sect. 2, the datasheet ADEV is converted to obtain PSD at frequency below 1 Hz. Figure 5 shows the PSD as a function of offset frequency spanning 10^{-5} to 10^{5} Hz, with low-frequency values derived from the ADEV conversion and high-frequency values taken directly from the datasheet [20].

Using the PSD in Fig. 5, two complementary noise series are generated to capture different timescales of clock behavior. A coarse series with a larger step size represents long-term drift across the entire propagation duration, while a fine series with a small step size captures short-term fluctuations within individual observation passes. For example, simulating an entire 2-day mission at the fine step of 1 μs would require over 1.7×10^{11} points, which is computationally prohibitive. By splitting the simulation into a coarse series with 1.7×10^{5} points and fine series of 1.6×10^{7} points per observation window, both low- and high-frequency noise

are accurately captured without excessive memory or processing demands. Figure 6a and b show the example series. Both series are combined to represent realistic timing errors at all relevant scales. For the Microchip CSAC, this corresponds to absolute timing errors of tens of nanoseconds over second-level integration times and sub-nanosecond errors at microsecond scales.

Although ADEV is not ideal for representing high-frequency noise components, which often follow power laws with $\alpha > 1$, it is used here solely for validation. The noise time series generated from the PSD is converted to an ADEV curve to enable direct comparison with the datasheet. Figure 7 shows that the fine and coarse noise series agree well near the 1 s transition region and align with the datasheet values. This consistency confirms the validity of the methodology for producing a coherent noise time series.

The corresponding power-law behavior of the simulated noise is summarized in Eq. (38).

$$\sigma_y(\tau) \propto \tau^{\mu/2}, \text{where } \frac{\mu}{2} \approx \begin{cases} -0.97, & \text{for } \tau \leq 3 \times 10^{-3}\,\text{s} \\ +0.25, & \text{for } 3 \times 10^{-3} \leq \tau < 0.06\,\text{s} \\ -0.5, & \text{for } \tau > 0.06\,\text{s} \end{cases}. \tag{38}$$

The datasheet reports phase noise with spectral slopes $\alpha \in [-2.5, 1.5]$ and $\mu \approx -1$. The simulation reproduces the expected behavior for short ($\tau < 3 \cdot 10^{-3}$ s) and long ($\tau > 0.06$ s) integration times. For intermediate integration times, the simulated noise shows $\mu = 0.5$ (or $\alpha = -1.5$), deviating from the input $\alpha = -2.5$, illustrating that ADEV does not fully capture noise contributions in certain low-frequency regimes. Nevertheless, the overall validation confirms that the generated time series accurately represent both short- and long-term clock noise suitable for subsequent mission simulations.

In principle, the expected contribution of clock noise to range error can be estimated from the Allan deviation as $\epsilon_{k,c} \propto \sigma_y(\tau)\,\tau$. However, since ADEV does not fully capture the high-frequency noise components relevant to short integration times, this relation is only indicative. Therefore, in the simulations, the full time series similar to shown in Fig. 6 is added as noise to the inter-satellite range observables.

4.2 Orbit

This subsection presents the results of the orbital propagation of CubeSats C1 and C2 around 99942 Apophis over an 8-day simulation period. Two distinct orbital configurations were considered to investigate the influence of relative satellite geometry on inter-satellite laser ranging performance: the coplanar and non-coplanar configurations. The initial conditions for both scenarios are given in Table 3.

In the coplanar configuration, both satellites share nearly identical orbital elements and differ only in initial true anomaly. This results in a phased formation in which the satellites follow the same orbital path but are separated along the track, producing a nominally coplanar orbit (Figs. 8a and 9a). Over the first 3.5 days, the inter-satellite separation oscillates around 1 km. The separation then gradually decreases over the next 2 days before expanding again, eventually settling into another oscillatory pattern around 400 m (Fig. 10a). These variations are primarily due to the strong gravitational influence of Apophis at this low orbital altitude.

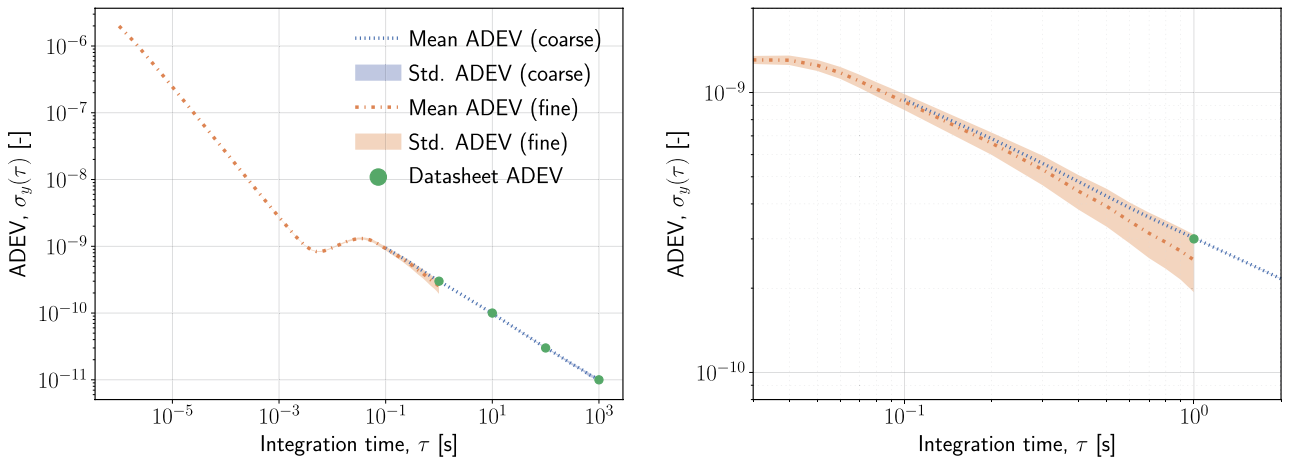

(a) Overview across all integration times.

(b) Zoomed-in view for overlapping region for integration times 0.4–2 s.

Fig. 7 ADEV as a function of integration time for Microchip CSAC from simulated fine and coarse time series to verify noise-statistics conversion. Mean and standard deviation of ADEV are obtained from 1000 Monte Carlo runs.

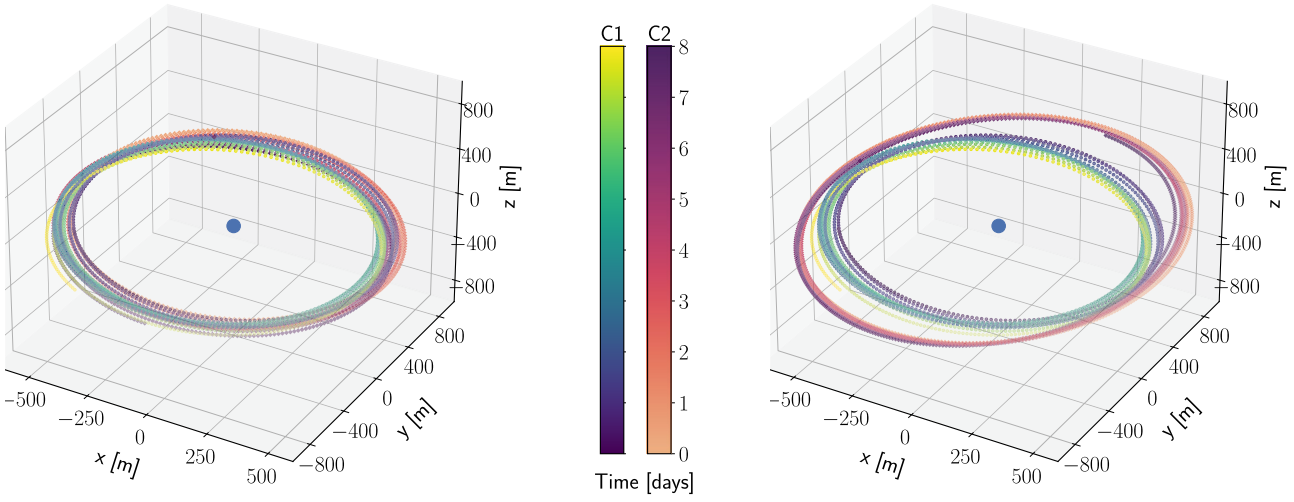

(a) Coplanar orbit configuration.

(b) Non-coplanar orbit configuration.

Fig. 8 Three-dimensional orbital trajectories of CubeSats C1 and C2 in the coplanar and non-coplanar configurations propagated over 8 days. The blue circle represents the center of the frame, Apophis.

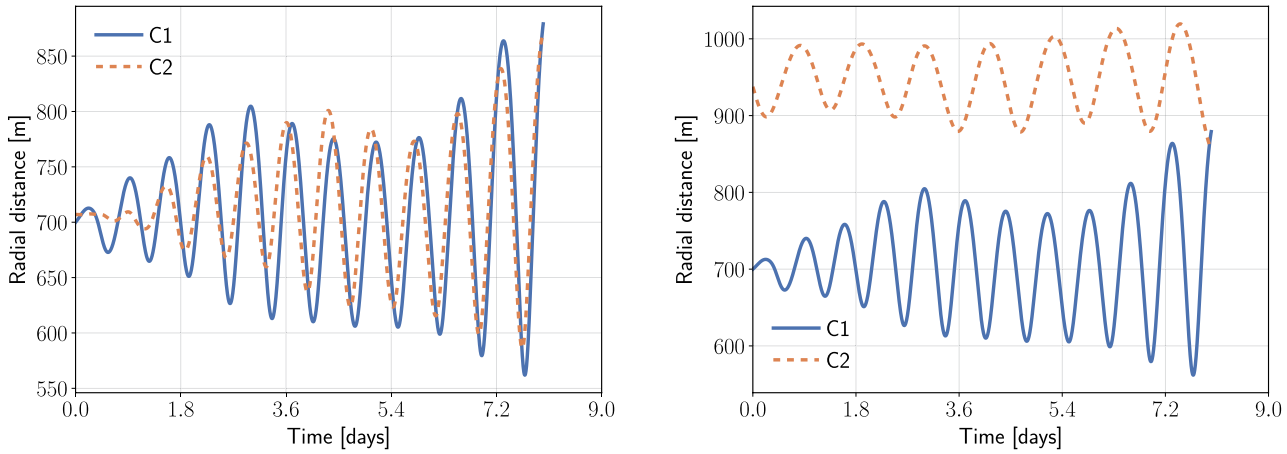

(a) Radial distance evolution for the coplanar orbit configuration.

(b) Radial distance evolution for the non-coplanar orbit configuration.

Fig. 9 Time evolution of the radial distance of CubeSats C1 and C2 from center of mass of Apophis for the coplanar and non-coplanar orbit configurations.

In the non-coplanar configuration (Fig. 8b), C2 is placed on a distinct orbital plane, producing wider spatial separation and out-of-plane relative motion of the satellites. The inter-satellite distance in this case (Fig. 10b) is more stable, varying periodically between 300 and 1700 m. The greater stability is linked to the higher altitude of C2, where gravitational perturbations are weaker. Additionally, the non-coplanar geometry improves the geometric constraints for inter-satellite ranging by increasing the baseline diversity in the out-of-plane direction. This enhances sensitivity in estimating the radial distance and gravitational parameter of Apophis, as the line-of-sight vectors from the two satellites to the asteroid span a larger volume, reducing dilution of precision (DOP) in the radial component and improving observability of the along-track gravitational perturbation.

Both configurations exhibit radial distance oscillations, with larger amplitudes in the coplanar case due to the satellites closer proximity to Apophis (Fig. 9). The inter-satellite time of flight remains on the order of microseconds in both cases. Based on their geometry, the coplanar configuration is expected to be more sensitive to short-term near-field dynamics, whereas the non-coplanar configuration may provide improved stability and measurement geometry for gravitational parameter estimation.

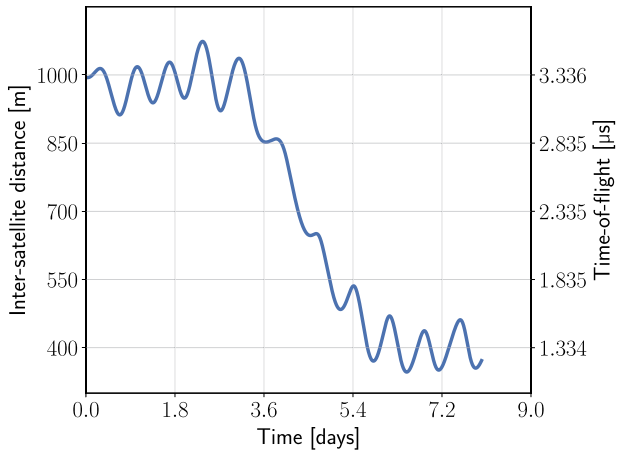

(a) Inter-satellite distance evolution for the coplanar orbit configuration.

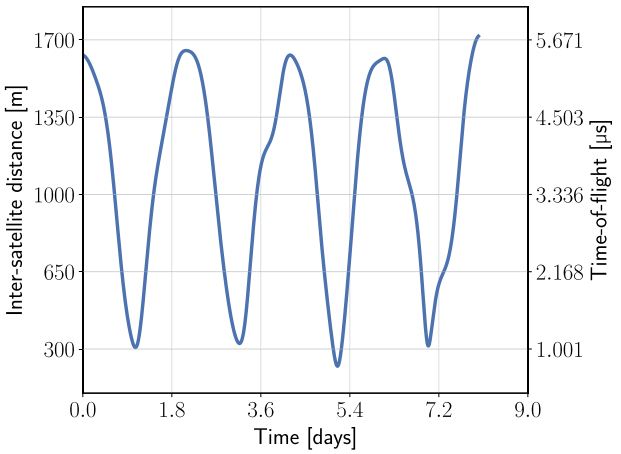

(b) Inter-satellite distance evolution for the non-coplanar orbit configuration.

Fig. 10 Time evolution of the inter-satellite distance between CubeSats C1 and C2 for coplanar and non-coplanar orbit configurations.

4.3 Link analysis

The cadence of LCT-based inter-satellite range measurements is fundamentally constrained by the bit rate of the optical link. As discussed in Sect. 3.3.1, the maximum achievable bit rate is determined by the available hardware bandwidth and the chosen modulation scheme. For the selected OOK modulation ($\eta = 1\ bits/s/\mathrm{Hz}$) and a hardware bandwidth of 500 MHz, the maximum achievable bit rate is 500 Mbps, corresponding to a frame duration or measurement step of 19.008 µs. However, since the measurement timing is governed by discrete 10 MHz clock ticks, the measurement step must be an integer multiple of the clock period. To satisfy this constraint, a rounded measurement step of 20 µs is adopted, resulting in a bit rate of 475.2 Mbps and an effective data rate of 422.4 Mbps according to the ESTOL protocol specifications given in Table 5 [35]. This slight rounding introduces a negligible difference and does not significantly affect the range noise or estimation results.

Using this bit rate, the inter-satellite laser communication link is analyzed under worst-case distance scenarios to ensure reliable ranging and data exchange. For the coplanar configuration, the maximum separation is 1074 m, while for the non-coplanar configuration it is 1720 m. The corresponding link budgets are summarized in Table 6. The computed link margins of 22.15 dB for the coplanar and 18.07 dB for non-coplanar configurations confirm reliable performance with a BER of 10^{-6}.

While the full link budget confirms reliable operation under worst-case distances and chosen BER, the key aspect relevant for orbit determination is the measurement step (frame duration). This sets the cadence of inter-satellite range observations and the sampling of clock noise in the simulated observables, which directly influences the estimation errors analyzed in the Monte Carlo simulations.

Table 6 Laser communication link budget parameters and computed link margin for the coplanar and non-coplanar orbit configurations at bit rate of 475.2 Mbps and BER of 10^{-6}

	Coplanar		Non-coplanar	
	W	dB	W	dB
P_t	0.2	−6.99	0.2	−6.99
G_t	1.42×10^9	91.53	1.42×10^9	91.53
μ_t	0.7	−1.55	0.7	−1.55
G_r	6.94×10^8	88.42	6.94×10^8	88.42
μ_r	0.7	−1.55	0.7	−1.55
L_p	0.9	−0.46	0.9	−0.46
L_{fs}	1.29×10^{-20}	−198.79	5.15×10^{-21}	−202.88
P_r	1.15×10^{-3}	−29.39	0.45×10^{-3}	−33.47
P_n	7.83×10^{-7}	−61.06	4.89×10^{-7}	−63.10
SNR	1.46×10^3	31.67	9.18×10^2	29.63
P_{req}	7.14×10^{-6}	−51.54	7.14×10^{-6}	−51.54
LM	164.09	22.15	64.19	18.07

4.4 Estimation results

This section presents the outcomes of orbit estimation conducted using the simulation framework introduced in Sect. 3.6. Two types of measurements are considered: Earth-based Doppler tracking of both satellites and inter-satellite LCT-based range observations, each subject to the noise sources described in Sect. 3.4.

To isolate the influence of clock-induced errors, the transmission offset δt is systematically varied between 1 µs and 10^5 s (27 h), thereby modifying the effective integration

time over which two-way clock noise accumulates. For each value of δt, 1000 independent Monte Carlo simulations are performed, providing statistically robust results despite the stochastic nature of both the noise processes and the batch least-squares estimation algorithm.

The results are presented in two main parts. First, the effect of transmission offset on two-way range errors is characterized for all space-qualified clocks listed in Sect. 2.2. Second, the evolution of true estimation errors in the x, y, and z position components and in the gravitational parameter μ is analyzed over the observation arc for a single clock, the Microchip CSAC, highlighting the contribution of ISLs to orbit determination accuracy in both orbit configurations (coplanar and non-coplanar).

4.4.1 Effect of transmission offset on range error

This subsection examines how the transmission offset δt affects two-way inter-satellite range error for six space-qualified clocks listed in Sect. 2.2. Each data point is derived from 1000 Monte Carlo simulations per clock and δt value, ensuring statistical robustness. Figure 11 shows the resulting range error trends, with horizontal reference lines at 0.102 m (due to 240 ps detector jitter) and 0.085 m (due to 200 ps time-tagging uncertainty), representing system-limited errors. Not all clocks provide ADEV data up to 10^5 s timescales: the Microchip CSAC datasheet ends at $\tau \approx 1000$ s, and the Safran MiniRAFS and Safran RAFS at $\tau \approx 10^4$ s.

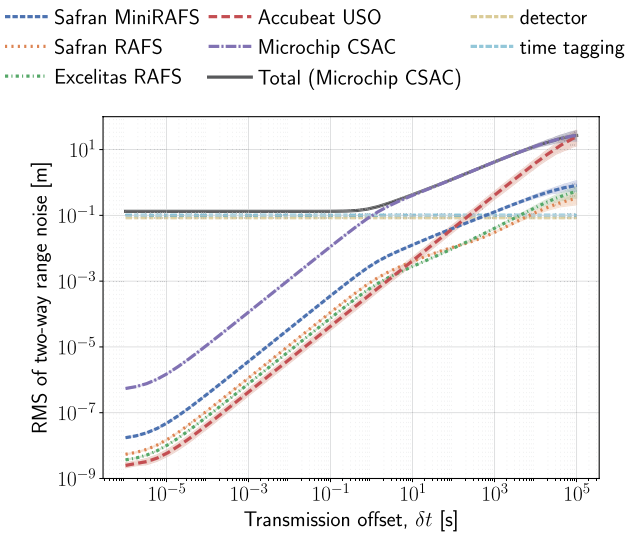

Fig. 11 Variation of two-way inter-satellite range noise with transmission offset, arising from errors in the clock, detector, and time-tagging for six different space-qualified clocks. Shaded regions indicate ±1 standard error of the RMSE. Due to the large number of runs, the standard error is very small, so the shading is barely visible on this scale. **Note**: Datasheet ADEV ends at $\tau \lesssim 10^3$ s (Microchip CSAC) and $\tau \lesssim 10^4$ s (Safran). Values beyond these limits are extrapolated and are illustrative only.

Beyond these limits, the corresponding ADEV curves are extrapolated by holding the final reported value constant. This assumption allows exploration of long-offset behavior but does not represent validated long-term clock performance. In reality, most oscillators transition to higher-slope noise processes at large τ (e.g., flicker walk or random walk for quartz oscillators, and flicker-to-random-walk transitions for rubidium clocks), which would increase phase and range noise relative to the flat extrapolation used here. Thus, the long-δt portions of Fig. 11 should be interpreted as optimistic lower bounds that still preserve the qualitative trend: less stable clocks exhibit larger errors at shorter offsets and degrade more rapidly as transmission offsets increase.

All clocks follow a similar pattern: range errors increase with δt, showing a noticeable change in slope near 1 s. Each clock exceeds the system-limited error at a characteristic δt, reflecting its inherent stability. For $\delta t \lesssim 10$ s, all clocks maintain a two-way range error below 0.1 m, except the Microchip CSAC, which reaches this threshold at $\delta t = 1$ s.

In general, larger clocks achieve better stability, illustrating the trade-off between compactness and performance. The Accubeat Ultra-stable Oscillator (USO) is an exception, achieving errors comparable to larger clocks for $\delta t \lesssim 10$ s despite its small form factor (< 2U). This is enabled by its ultra-low phase noise quartz crystal oscillator, achieved through a high-Q resonator and low-noise sustaining amplifier design, combined with active double-oven thermal stabilization that maintains sub-mK temperature control over integration times of 1–1000 s, as developed for the JUICE mission's 3GM experiment [22].

The Microchip CSAC is selected for further orbit estimation due to its widespread use in small satellites and low SMaP requirements. For this clock, the figure shows that at short transmission offsets ($\delta t \lesssim 1$ s), range error stabilizes around 0.132 m, dominated by detector jitter and time-tagging uncertainty. At longer offsets ($\delta t \gtrsim 1$ s), clock noise becomes the dominant error source. Note that for offsets longer than 1000 s, this analysis relies on extrapolated ADEV values beyond the datasheet, which may underestimate true long-term clock noise.

These results suggest that the choice of clock should balance size, stability, and mission requirements. For short transmission offsets ($\delta t \lesssim 10$ s), where system noise dominates, compact clocks such as the Microchip CSAC or Accubeat USO achieve sub-decimeter range errors while imposing minimal SMaP (< 2U, low power). For longer offsets ($\delta t \gtrsim 10$ s) where sub-meter precision is required, larger, high-stability clocks such as Safran RAFS or Excelitas USO are recommended, achieving errors in the 0.01–0.05 m range but with increased SMaP (3–4U, higher power), illustrating a clear trade-off between precision and spacecraft resources. For small satellites with stringent SMaP constraints, the Microchip CSAC provides a practical compromise, offering

acceptable performance at short integration times while highlighting the limitations imposed by clock noise at longer offsets. Selecting a clock thus requires considering both the expected operational transmission offsets and the precision demands of the mission.

It should be noted that the analysis relies on manufacturer datasheet ADEV values, which reflect nominal laboratory conditions; in-flight performance may differ due to environmental factors such as temperature variations, radiation, or mechanical stress. While the relative stability ranking across clock types is expected to remain robust, absolute ranging errors could deviate from these predictions. All clocks studied are space-qualified or flight-proven, but final performance should be validated through thermal-vacuum testing, radiation exposure, or in-flight calibration.

4.4.2 Effect of transmission offset on orbit estimation

The initial states of both CubeSats were estimated over an 8-day propagation arc. To isolate the impact of ranging precision on orbit determination, a Doppler-only configuration—without ISL measurements—is first considered as the baseline. Estimation accuracy in all cases is assessed in the radial–tangential–normal (RTN) reference frame, which is defined relative to the center of mass of Apophis, with the radial (R) axis along the position vector, the tangential (T) axis along the velocity vector, and the normal (N) axis perpendicular to the orbital plane.

For the Doppler-only case, the truth and estimation models are identical; hence, covariance analysis is sufficient to capture the full error distribution, and no Monte Carlo simulations are required. The results presented for this configuration are therefore the formal errors obtained directly from the covariance matrix.

When ISL measurements are included alongside Doppler tracking, full orbit estimation is performed. Accuracy is quantified using the RMSE of the true errors in position and gravitational parameter μ, computed from Monte Carlo simulations as defined in Eq. (39):

$$\text{RMSE}, R_k = \sqrt{\frac{1}{N}\sum_{i=1}^{N} e_{k,i}^2}, \tag{39}$$

where $e_{k,i}$ is the true error of the estimated parameter k from the i-th Monte Carlo run at the initial epoch, and $N = 1000$ is the number of runs. The resulting RMSE values for both satellites and both orbital configurations are shown in Fig. 12.

Doppler-only measurements result in true position errors exceeding 1 m across all RTN components for both satellites and orbital configurations. For measurements involving ISL, the variation of the true errors with the transmission offset closely follows the total noise profile of the range measurements, as illustrated in Fig. 11. For transmission offsets shorter than 1s, sub-meter inter-satellite range precision reduces true errors from the 1 m-level to the 0.1 m level in the coplanar configuration, reflecting an improvement of approximately one order of magnitude. Beyond 1 s, clock noise becomes the dominant source of error, causing a gradual increase in true errors. When the transmission offset exceeds 10^4 s (≈ 2.7 h), true errors surpass those of the Doppler-only baseline, indicating that clock-induced errors degrade rather than improve the orbit estimation. This degradation arises because, at such long transmission offsets, the combined effects of clock noise and orbital motion cause the measured ranges to lose their strong correspondence with the satellites instantaneous positions, thereby reducing their information content and leading to higher estimation errors.

Incorporating ISL range measurements significantly improves orbit estimation accuracy in both coplanar and non-coplanar configurations, but the distribution of improvement across RTN components depends on both Doppler sensitivity and ISL geometry. In the coplanar case, Earth-based Doppler is most sensitive along the normal direction, partially constrains tangential motion, and provides very little information along the radial direction. The ISL vector is mostly aligned with the radial–normal plane, so the largest improvements occur in the radial and normal components, while the tangential component, already moderately constrained by Doppler, benefits less. In the non-coplanar configuration, Doppler strongly constrains radial motion, moderately constrains normal, and weakly constrains tangential motion. The out-of-plane ISL vector provides additional geometric information in all directions, with the largest enhancement in the radial component, followed by normal and tangential. Overall, the non-coplanar geometry improves observability across all state components, reduces parameter correlations, and further enhances the robustness and accuracy of the orbit estimation, yielding lower errors compared to the coplanar case. This behavior is clearly reflected in the RMSE trends shown in Fig. 12.

Similar trends are observed in the estimation of the gravitational parameter μ of Apophis, as shown in Fig. 13. In the coplanar configuration, ISL-enabled cases with transmission offsets lower than 1s reduce true errors in μ to 1.5×10^{-3} m^3/s, corresponding to a fractional uncertainty of approximately 0.042%, more than one order of magnitude lower than the Doppler-only baseline of 0.02 m^3/s (0.565%). The non-coplanar configuration achieves an even greater improvement, with true errors reaching 2×10^{-5} m^3/s (fractional uncertainty 0.00057%), exceeding two orders of magnitude reduction. Notably, even at large transmission offsets ($\delta t = 1000$ s), the non-coplanar configuration maintains errors more than one order of magnitude below the baseline, demonstrating the robustness of the out-of-plane geometry in preserving parameter observability despite

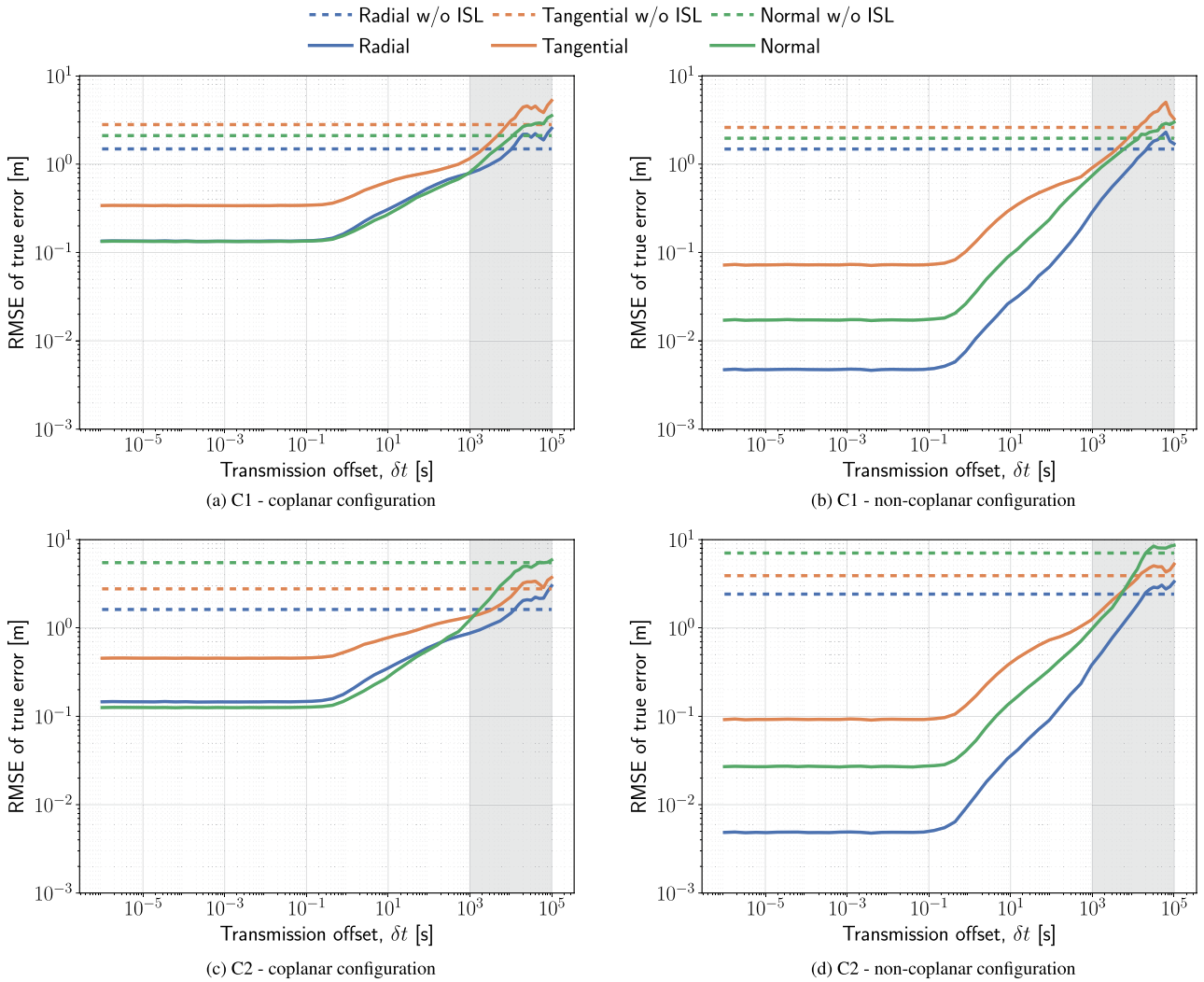

(a) C1 - coplanar configuration

(b) C1 - non-coplanar configuration

(c) C2 - coplanar configuration

(d) C2 - non-coplanar configuration

Fig. 12 Root mean square true position errors in the RTN frame for C1 and C2 in coplanar and non-coplanar configurations as a function of transmission offset. Shaded regions around the curves indicate ±1 standard error of the RMSE. Due to the large number of runs, the standard error is very small (approximately two orders of magnitude smaller than the RMSE), so the shading is barely visible at this scale. The vertical shaded region highlights the portion of the curves corresponding to extrapolated noise.

increased clock noise. These results are consistent with the positional error trends discussed earlier, where the non-coplanar configuration also showed higher accuracy across RTN components.

Overall, the incorporation of inter-satellite range measurements substantially improves the estimation of both position and μ, with the non-coplanar configuration offering sustained benefits across a broad range of transmission offsets. These insights are valuable for any future mission whose scientific objectives rely on high-precision tracking, as improved measurement accuracy directly enhances the ability to determine small-body masses, gravitational fields, and dynamical environments, and supports high-fidelity modeling for exploration and formation-flying operations. However, practical considerations such as increased system complexity and clock synchronization challenges must also be taken into account.

4.5 Discussion

The results presented demonstrate the capabilities of two-way LCT-based ranging for a formation of two satellites operating in the gravitationally complex environment of the near-Earth asteroid 99942 Apophis. The analysis underscores the strong interdependence between clock stability, orbital geometry, and the achievable precision of inter-satellite range measurements as seen from Figs. 11 and 12. The utility of ISL is context-dependent: it provides the greatest benefit along directions where Earth-based Doppler tracking is weakest. Even with continuous Earth-based tracking

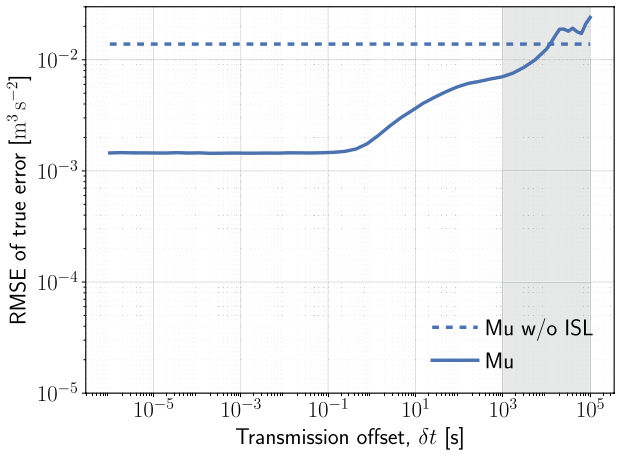

(a) Coplanar configuration.

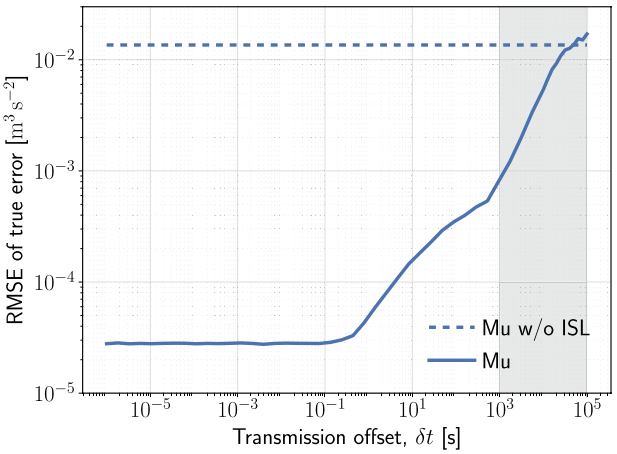

(b) Non-coplanar configuration.

Fig. 13 Root mean square true errors in the gravitational parameter μ for coplanar and non-coplanar configurations as a function of transmission offset. Shaded regions around the curves indicate ± 1 standard error of the RMSE. Due to the large number of runs, the standard error is very small (approximately two orders of magnitude smaller than the RMSE), so the shading is barely visible at this scale. The vertical shaded region highlights the portion of the curves corresponding to extrapolated noise.

around Apophis, ISL enhances estimation of certain state components as seen from Fig. 12. In missions with limited tracking opportunities, such as planetary moon operations or deep-space constellations, ISL can enhance state estimation by providing measurements in regions with sparse Earth-based data. These results highlight that the benefit of ISL is maximized when it complements the strengths and limitations of existing tracking data, although pointing and acquisition requirements for optical terminals may pose practical challenges.

Beyond geometry, the orbit determination performance in LCT-aided inter-satellite ranging also depends on the measurement integration time δt. For short integration times ($\delta t \lesssim 1$s), performance improvements saturate, as high-frequency noise is already well-averaged within the measurement window. Conversely, for very long integration times ($\delta t \sim 1000$ s), performance degrades as low-frequency clock errors begin to dominate. In typical mission operations with continuous data transmission, δt values are usually shorter than a second, meaning the choice of clock is less critical, since system-level errors from time-tagging electronics and detector noise dominate. However, for missions where communication alternates between satellites in different observation windows, integration times can reach 1000s, which can benefit from more stable clocks. Figure 11 illustrates how different clock types influence this behavior: more stable clocks (e.g., Excelitas or Quartzlock) maintain good performance at longer δt, whereas less stable clocks (e.g., CSAC) degrade earlier, highlighting the importance of matching the integration time to the clock characteristics and mission profile.

From a practical standpoint, these results provide guidelines for mission designers. For short transmission offsets ($\delta t \lesssim 1$s), compact clocks such as the Microchip CSAC or Accubeat USO deliver sub-decimeter performance with minimal SMaP impact. In this regime, system-level errors from detector jitter and time-tagging dominate, indicating that upgrading to a higher-stability oscillator may offer limited benefit. For longer transmission offsets ($\delta t \gtrsim 1$s), achieving sub-meter precision requires higher-stability clocks such as Safran RAFS or Excelitas USO. The results also suggest approximate thresholds where system-level noise dominates over clock-induced errors, providing actionable guidance for selecting integration times and clock classes tailored to mission objectives.

The methodology developed here is broadly applicable across different clock types. While the estimation analysis focused on the Microchip CSAC, a standard oscillator used in small satellites, other state-of-the-art space-qualified clocks have been evaluated, providing estimates of expected two-way range precision across different integration times as shown in Fig. 11. Selecting an appropriate clock for a given mission requires considering both its frequency stability and the achievable precision of the rest of the timing system. Unless these subsystems support clock-level or better precision, upgrading to a higher-end oscillator yields limited gains, illustrating the strong coupling between subsystem performance and oscillator choice.

These considerations naturally lead to practical implications for mission planning. The type of LCT considered in this study is most likely to be deployed on small satellite platforms such as CubeSats or microsats, where compact

size, mass, and power budgets are critical. Larger, more stable oscillators, such as USOs, are more suitable for flagship missions, where mass and power constraints are relaxed. Power budgeting is critical not only for the clock itself but also for auxiliary electronics needed for high-precision time-tagging of the laser communication signal, which can substantially increase overall power demand. Therefore, a trade-off must be made between clock stability, system-level performance, and onboard resource constraints. In addition, periodic clock calibration with ground stations could be performed to further improve ranging performance and mitigate long-term drift.

It should be noted that the current study assumes noise-free link acquisition and neglects photon shot noise, background radiation variability, and pointing losses beyond the static budget. In practice, these factors may increase the overall range error and shift the thresholds where system-level noise dominates over oscillator-induced errors. While the analysis provides a robust baseline for inter-satellite ranging performance, designers should account for these additional noise sources in detailed mission simulations to ensure conservative system sizing and error budgeting.

In addition to system design considerations, it is also important to account for how clock noise is modeled in actual flight data. When clock noise is the dominant contributor to range error, orbit determination can incorporate stochastic clock models that capture key noise types such as white noise, flicker frequency noise, and random walk [44]. For LEO satellites, 2.5-state clock models are commonly used to estimate bias and drift alongside orbital states, improving orbit determination accuracy [45, 46]. The choice of state model depends on the stability of the clock, with more states required for less stable clocks or longer missions where frequency drift can become significant.

Overall, this study provides a generalizable framework for understanding the interplay between oscillator performance, system-level noise, ISL geometry, and orbit determination accuracy. The insights gained are applicable to any mission where precise tracking is critical for science objectives—whether for asteroid mass and density determination, planetary gravity recovery, formation flying, or deep-space navigation [2]. Beyond the specific Apophis scenario, the principles established here offer practical guidance for designing inter-satellite tracking systems that maximize information content while respecting spacecraft size, mass, and power constraints, helping ensure mission designs that remain both efficient and scientifically robust.

5 Conclusions and future work

This study demonstrates the capabilities and limitations of two-way LCT-based inter-satellite ranging for CubeSat formations operating around a near-Earth asteroid. A central outcome is the detailed characterization and modeling of clock-induced timing errors, providing a methodology for incorporating clock noise into orbit determination algorithms and predicting its propagation into estimation uncertainties. For short integration times, PSD-based representations capture high-frequency behavior, while for longer timescales, time-domain variance or ADEV is appropriate. Near 1 s integration times, both representations should be combined to model low- and high-frequency contributions. When clock noise dominates, colored noise should be incorporated into simulated range measurements to accurately reflect its impact. By systematically analyzing the impact of clock stability, transmission offset, and orbital geometry, the study quantifies how ISLs improve orbit determination accuracy and reduce errors in key parameters, including the gravitational parameter μ. The results highlight that ISL benefits are maximized along directions weakly constrained by Earth-based Doppler, while subsystem-level noise—such as detector jitter and time-tagging—can limit achievable precision even with high-performance clocks.

The methodology provides a framework to evaluate clock selection, link geometry, and system-level trade-offs for a wide range of missions and orbital configurations. These insights offer practical guidance for future missions whose science objectives critically depend on precise satellite tracking, enabling informed decisions regarding oscillator performance, link design, and spacecraft resource allocation.

Future studies could extend this analysis to multi-satellite constellations and more complex orbital environments, such as libration point orbits or planetary moons, where ISL geometry and dynamics are more intricate. Incorporating realistic ground station duty cycles, data gaps, and colored noise would further refine predictions for orbit determination performance. Additional work should include a comprehensive assessment of LCT hardware contributions to total range error, with particular focus on time-tagging jitter and detector timing jitter, alongside photon noise, receiver bandwidth, and filtering effects. Investigating adaptive filtering and weighting strategies to mitigate long-transmission-offset clock noise, as well as the trade-offs between clock performance, detector electronics, and spacecraft resource budgets, would further enhance mission planning. Finally, in-flight validation using operational LCT payloads is essential to confirm model predictions and guide the design of future high-precision inter-satellite ranging missions.

Convergence conditions for Allan deviation integral

The AVAR $\sigma_y^2(\tau)$ can be expressed in terms of the PSD $S_y(f)$ as:

$$\sigma_y^2(\tau) = \int_0^\infty S_y(f)|H_y(f)|^2\, df = 2\int_0^\infty h_\alpha f^\alpha \left[\frac{\sin^4(\pi\tau f)}{(\pi\tau f)^2}\right] df, \tag{A. 1}$$

where $h_\alpha f^\alpha$ models the PSD with spectral index α, and $|H_y(f)|^2$ is the AVAR filter transfer function. For this integral to be well-defined and converge, it must be finite at both the low-frequency ($f \to 0$) and high-frequency ($f \to \infty$) limits. To analyze this, consider the asymptotic behavior of the integrand in the following equation:

$$\sigma_y^2(\tau) \propto \int_0^\infty f^\alpha \frac{\sin^4(\pi\tau f)}{(\pi\tau f)^2} df. \tag{A. 2}$$

Using asymptotic approximations near the limits, the integrand behaves as:

$$\sigma_y^2(\tau) \propto \begin{cases} \displaystyle\int^\infty f^{\alpha-2}\, df, & f \to \infty, \\ [12pt] \displaystyle\int_0 f^{\alpha-2}(\pi\tau f)^4\, df \sim \int_0 f^{\alpha+2}\, df, & f \to 0. \end{cases} \tag{A. 3}$$

The convergence of integrals of the form $\int x^p\, dx$ requires:

$$\begin{cases} p < -1, \text{ for } x \to \infty \\ p > -1, \text{ for } x \to 0 \end{cases} \implies \begin{cases} \alpha - 2 < -1 \implies \alpha < 1\,, \\ \alpha + 2 > -1 \implies \alpha > -3\,. \end{cases} \tag{A. 4}$$

Thus, the analytical expression to obtain AVAR from PSD is valid in the spectral range $-3 < \alpha < 1$.

Noise budget

The SNR is the ratio of the power of the received signal (P_r) to the power of the noise (P_n) at the receiver. The noise power can be expressed in terms of the noise equivalent power (NEP) and the noise variance σ_n^2 by:

$$P_n = \text{NEP} \cdot \sqrt{B} = \frac{\sigma_n}{G \cdot R_d \cdot \sqrt{B}} \cdot \sqrt{B} = \frac{\sigma_n}{G \cdot R_d}\,, \tag{B.1}$$

where G is the detector gain and R_d is the detector responsivity given by:

$$R_d = \frac{\eta \cdot q_e \cdot \lambda}{h \cdot c}\,, \tag{B.2}$$

where η is the detector quantum efficiency, λ is the wavelength of light, q_e is the electron charge, h is the Planck's constant, and c is the speed of light.

The main sources of this noise are dark current (σ_{dc}), background radiation (σ_{bg}), quantum (σ_q) and thermal noise (σ_t). The total noise variance is the sum of the individual contributions:

$$\sigma_n^2 = \sigma_{dc}^2 + \sigma_{bg}^2 + \sigma_q^2 + \sigma_t^2\,. \tag{B.3}$$

Each term is calculated as follows:

$$\sigma_{dc}^2 = 2\, q_e\, I_{dc}\, B\, F\, G^2, \tag{B.4}$$

$$\sigma_{bg}^2 = 2\, q_e\, R_d\, P_{bg}\, B\, F\, G^2, \tag{B.5}$$

$$\sigma_q^2 = 2\, q_e\, R_d\, P_r\, B\, F\, G^2, \tag{B.6}$$

$$\sigma_t^2 = I_{amp}^2\, B, \tag{B.7}$$

where I_{dc} is the dark current, B is the receiver bandwidth, F is the excess noise factor of the detector, P_{bg} is the background optical power, and I_{amp} is the amplifier current noise. The background power P_{bg} is computed from the spectral irradiance:

$$P_{bg} = L(\lambda, T) \cdot \Delta\lambda \cdot \Omega \cdot \pi(D_r/2)^2 \cdot \eta \cdot L_r, \tag{B.8}$$

$$L(\lambda, T) = \frac{2hc^2}{\lambda^5} \cdot \frac{1}{\exp\left(\frac{hc}{\lambda k_B T}\right) - 1}, \tag{B.9}$$

where $L(\lambda, T)$ is the Planck spectral radiance, $\Delta\lambda$ is the optical filter bandwidth, Ω is the solid angle of the receiver field of view, D_r is the receiver aperture diameter, k_B is the Boltzmann's constant, and L_r accounts for additional optical losses.

Acknowledgements The authors would like to thank the Dutch Research Council (NWO) for their support in funding the Perspective Project P19-13, "Optical Wireless Super Highways". The authors also gratefully acknowledge the guidance and encouragement of Dr. ir. Angelo Cervone (TU Delft), whose support and advice contributed to the successful completion of this work. We thank Michael K. Plumaris (Sapienza University of Rome) for clarifying aspects of the Timmer & Koenig algorithm relevant to this study.

Author Contributions **RJ** conceived the study, developed the methodology, performed the simulations, and wrote the manuscript. **DD** and **SS** provided supervision, guidance throughout the research, and critical review of the manuscript.

Data Availability The data required to reproduce the results of this study are contained within the manuscript. All simulations were performed using the open-source Tudat Python library (documentation: https://tudat-space.readthedocs.io, source code: https://github.com/tudat-team/tudat-bundle). The simulation scripts supporting this work are available from the corresponding author upon reasonable request.

Declarations

Conflict of interest The authors declare no conflict of interest.

References

1. Zhang, J.Y., Ming, M., Jiang, Y.Z., et al.: Inter-satellite laser link acquisition with dual-way scanning for Space Advanced Gravity Measurements mission. Rev. Sci. Instrum. **89**(6), 064501 (2018). https://doi.org/10.1063/1.5019433
2. Jain, R., Speretta, S., Dirkx, D., et al.: Inter-satellite tracking methods and applications: a comprehensive survey. Adv. Space Res. **74**(8), 3877–3901 (2024). https://doi.org/10.1016/j.asr.2024.08.022
3. Andrews, K., Hamkins, J., Shambayati, S., et al.: Telemetry based ranging. In: IEEE Aerospace Conference (2010). https://doi.org/10.1109/AERO.2010.5446926
4. Hamkins, J., Kinman, P., Xie, H., et al.: Telemetry ranging: concepts. Interplanetary Network Progress Report, 42-203, pp. 1–20. https://ui.adsabs.harvard.edu/abs/2015IPNPR.203C...1H (2015)
5. Hamkins, J., Kinman, P., Xu, Z., et al.: Telemetry ranging: laboratory validation tests and end-to-end performance. IPN Progress Report, 42-206. https://ui.adsabs.harvard.edu/abs/2016IPNPR.206D...1H (2016a)
6. Hamkins, J., Kinmany, P., Xie, H., et al.: Telemetry ranging: signal processing. Interplanetary Network Progress Report, 42–204. https://ui.adsabs.harvard.edu/abs/2016IPNPR.204D...1H (2016b)
7. Vilnrotter, V., Hamkins, J.: Telecommand/Telemetry ranging for deep-space applications. In: IEEE Aerospace Conference (1–10) (2019). https://doi.org/10.1109/AERO.2019.8742212
8. Turan, E., Speretta, S., Gill, E.: Performance analysis of crosslink radiometric measurement based autonomous orbit determination for cislunar small satellite formations. Adv. Space Res. **72**(7), 2710–2732 (2023). https://doi.org/10.1016/j.asr.2022.11.032
9. Stevens, M.L., Parenti, R.R., Willis, M.M., et al.: The lunar laser communication demonstration time-of-flight measurement system: overview, on-orbit performance, and ranging analysis. In: Free-Space Laser Communication and Atmospheric Propagation XXVIII (2016). https://doi.org/10.1117/12.2218624
10. Toyoshima, M.: Recent trends in space laser communications for small satellites and constellations. J. Lightwave Technol. **39**(3), 693–699 (2021)
11. Hartwig, O., Bayle, J.-B.: Clock-jitter reduction in lisa time-delay interferometry combinations. Phys. Rev. D. **103**, 123027. https://link.aps.org/doi/10.1103/PhysRevD.103.123027. https://doi.org/10.1103/PhysRevD.103.123027 (2021)
12. Grenfell, P.: Systems performance analysis for autonomous spacecraft navigation within satellite constellations using intersatellite optical communications links. Ph.D. thesis, Massachusetts Institute of Technology (2024)
13. Dellagiustina, D.N., Nolan, M.C., Polit, A.T., et al.: Osiris-apex: an osiris-rex extended mission to asteroid apophis. Planet. Sci. J. **4**(10) (2023). https://doi.org/10.3847/PSJ/acf75e
14. Lasagni Manghi, R., Zannoni, M., Gramigna, E., et al.: A radio science experiment for the ramses mission to apophis. In: Europlanet Science Congress 2024. **17** (2024). https://doi.org/10.5194/epsc2024-822
15. Rivkin, A.S., Cheng, A.F.: Planetary defense with the double asteroid redirection test (dart) mission and prospects. Nat. Commun. **14**(1) (2023). https://doi.org/10.1038/s41467-022-35561-2
16. Jones, G.H., Snodgrass, C., Tubiana, C., et al.: The comet interceptor mission. Space Sci. Rev. **220**(1) (2024). https://doi.org/10.1007/s11214-023-01035-0
17. Gramigna, E., Lasagni Manghi, R., Zannoni, M., et al.: The hera radio science experiment at didymos. Planet. Space Sci. **246**, 105906 (2024). https://doi.org/10.1016/j.pss.2024.105906
18. Riley, W.: Handbook of frequency stability analysis. Report National Institute of Standards and Technology (2008)
19. Nanyang Technological University Satellite Research Centre. Spatium—space precision atomic-clock timing utility mission. https://www.ntu.edu.sg/sarc/research-capabilities/satellites/spatium (2024). Accessed 14 Nov 2025
20. Microchip Technology Inc. Chip Scale Atomic Clock (CSAC). https://www.microchip.com/en-us/product/CSAC-SA45S (2025). Accessed 11 Aug 2025
21. Safran—Navigation & Timing MiniRAFS Rubidium Atomic Frequency Standard. https://safran-navigation-timing.com/product/minirafs-rb-atomic-frequency-standard/ (2025a). Accessed 11 Aug 2025
22. Shapira, A.: An ultra stable oscillator for the 3GM experiment of the JUICE mission. In: Proc. 2016 IEEE Int. Freq. Control Symp. (IFCS) (1–4) (2016). https://doi.org/10.1109/FCS.2016.7546760
23. AccuBeat. Ultra Stable Oscillator (USO) for deep space exploration. https://www.accubeat.com/uso (2025). Accessed 11 Aug 2025
24. Droz, F., Rochat, P., Wang, Q.: Performance overview of space rubidium standards. In: EFTF-2010 24th European Frequency and Time Forum (1–6) (2010). https://doi.org/10.1109/EFTF.2010.6533702
25. Safran—Navigation & Timing Rubidium Atomic Frequency Standard (RAFS). https://safran-navigation-timing.com/product/rafs/ (2025b). Accessed 11 Aug 2025
26. Excelitas Technologies Corporation.: Excelitas technologies celebrates 20 years of continuous, failure-free operations of its rafs aboard on-orbit gps-iir satellite. https://www.excelitas.com/de/press-release/excelitas-technologies-celebrates-20-years-continuous-failure-free-operations-its (2017). Accessed 14 Nov 2025
27. Excelitas Technologies Corporation.: Space-qualified rubidium atomic frequency standard clocks. https://www.excelitas.com/product/space-qualified-rubidium-atomic-frequency-standard-clocks(2025). Accessed 11 Aug 2025
28. De Marchi, F., Plumaris, M.K., Burt, E.A., et al.: An algorithm to estimate the power spectral density from allan deviation. IEEE Trans. Ultrason. Ferroelectr. Freq. Control **71**(4), 506–515 (2024). https://doi.org/10.1109/TUFFC.2024.3372395
29. Timmer, J., Konig, M.: On generating power-law noise. Astron. Astrophys. **300**(3), 707–710.<Go to ISI>://WOS:A1995RR43900006 (1995)
30. Greenhall, C.A.: FFT-based methods for simulating flicker FM. In: Proceedings of the 34th Annual Precise Time and Time Interval (PTTI) Systems and Applications Meeting, pp. 481–491. Reston, Virginia, NASA Jet Propulsion Laboratory (2002)
31. Morelli, A.C., Mannocchi, A., Giordano, C., et al.: Initial trajectory assessment of a low-thrust option for the ramses mission to (99942) apophis. Adv. Space Res. **73**(8), 4241–4253 (2024). https://doi.org/10.1016/j.asr.2024.02.005

32. Aljbaae, S., Sanchez, D., Prado, A., et al.: First approximation for spacecraft motion relative to (99942) apophis. Rom. Astron. J. **31**, 241–263 (2021)
33. Pravec, P., Scheirich, P., Durech, J., et al.: The tumbling spin state of (99942) apophis. Icarus **233**, 48–60 (2014). https://doi.org/10.1016/j.icarus.2014.01.026
34. Souchay, J., Lhotka, C., Heron, G., et al.: Changes of spin axis and rate of the asteroid (99942) apophis during the 2029 close encounter with earth: a constrained model. Astron. Astrophys. **617** (2018). https://doi.org/10.1051/0004-6361/201832914
35. Agency, European Space Japan Aerospace Exploration Agency (JAXA), & ESA Member States Industries. ESA specification for terabit/sec optical links (estol). https://connectivity.esa.int/sites/default/files/2025-07/ESTOL_air_interface_v2.2.pdf (2024). eSA UNCLASSIFIED—Releasable to the Public
36. Friis, H.T.: A note on a simple transmission formula. Proc. Inst. Radio Eng. **34**(5), 254–256 (1946). https://doi.org/10.1109/Jrproc.1946.234568
37. Moision, B., Wu, J., Shambayati, S.: An optical communications link design tool for long-term mission planning for deep-space missions. In: 2012 IEEE Aerospace Conference.<Go to ISI>://WOS:000309105301028 (2012)
38. Sesta, A., Durante, D., Boscagli, G., et al.: Atlas: orbit determination and time transfer for a lunar radio navigation system. Navigat.-J. Inst. Navigat. **72**(2) (2025). https://doi.org/10.33012/navi.701
39. Bauer, S., Hussmann, H., Oberst, J., et al.: Analysis of one-way laser ranging data to lro, time transfer and clock characterization. Icarus **283**, 38–54 (2017). https://doi.org/10.1016/j.icarus.2016.09.026
40. Buccino, D.R., Oudrhiri, K., Parisi, M., et al.: Precision of spacecraft doppler tracking at low signal-to-noise ratios. Radio Sci. **58**(7) (2023). https://doi.org/10.1029/2023RS007703
41. Dirkx, D.: Interplanetary laser ranging. Ph.D. thesis, Delft University of Technology (2015)
42. Kang, Z., Bettadpur, S., Nagel, P., et al.: Grace-fo precise orbit determination and gravity recovery. J. Geodesy **94**(9) (2020). https://doi.org/10.1007/s00190-020-01414-3
43. Dirkx, D., Fayolle, M., Garrett, G., et al.: The open-source astrodynamics tudatpy software—overview for planetary mission design and science analysis. EPSC2022, (EPSC2022-253) (2022)
44. Chan, F.C., Joerger, M., Pervan, B.: Stochastic modeling of atomic receiver clock for high integrity gps navigation. IEEE Trans. Aerosp. Electron. Syst. **50**(3), 1749–1764 (2014). https://doi.org/10.1109/Taes.2014.120402
45. Wang, K., El-Mowafy, A., Yang, X.: LEO satellite clock modeling and its benefits for LEO kinematic POD. Remote Sens. **15**(12) (2023). https://doi.org/10.3390/rs15123149
46. Ge, Y.L., Liu, Y.L., Lyu, D., et al.: Leo satellite clock modeling and its benefits for real-time leo ppp timing. Measurement **242** (2025). https://doi.org/10.1016/j.measurement.2024.116035